Marciniak-Kuczynski type modelling of the effect of Through-Thickness Shear on the forming limits of sheet metal

Philip Eyckens *,a, Albert Van Bael a,b and Paul Van Houtte a

aDepartment MTM, Katholieke Universiteit Leuven, Kasteelpark Arenberg 44 Bus 02450, BE-3001 Heverlee, Belgium
bIWT, KHLim (Limburg Catholic University College), Campus Diepenbeek, Agoralaan Gebouw B, Bus 3, BE-3590 Diepenbeek, Belgium

Abstract

The Marciniak-Kuczynski (MK) forming limit model is extended in order to predict localized necking in sheet metal forming operations in which Through-Thickness Shear (TTS), also known as out-of-plane shear, occurs. An example of such a forming operation is Single Point Incremental Forming. The Forming Limit Diagram (FLD) of a purely plastic, isotropic hardening material with von Mises yield locus is discussed, for monotonic deformation paths that include TTS. If TTS is present in the plane containing the critical groove direction in the MK model, it is seen that formability is increased for all in-plane strain modes, except equibiaxial stretching. The increase in formability due to TTS is explained through a detailed study of some selected deformation modes. The underlying mechanism is a change of the stress mode in the groove that results in a delay of the onset of localized necking.

Keywords: fracture mechanisms (A), metallic material (B), plates (B), stability and bifurcation (C), Forming Limit Curve

* Corresponding author. Philip.eyckens@mtm.kuleuven.be; Tel.: +32 16321305; fax: +32 16321990.

1 INTRODUCTION

The Marciniak-Kuczynski (MK) type of model is widely used as a framework to develop models for the prediction of localized necking in sheet metal forming, though it is by no means the only model. Other types include the bifurcation type of model, see e.g. Hashiguchi and Protasov (2004), and the perturbation type of model, as in Boudeau et al. (1998).

Since the original paper of Marciniak and Kuczynski (1967), understanding of the localized necking phenomenon has greatly advanced. In the original paper, the existence of an initial groove with diminished thickness, of infinite length and oriented along the minor strain direction, was assumed in order to predict the forming limit of monotonic strain paths in the right-hand side of the Forming Limit Diagram (FLD). Later on, as in Hutchinson and Neale (1977a), it was extended to cover the whole range of the FLD by considering all possible initial orientations of the groove and retaining the lowest value of the major strain at the onset of localized necking as the limit strain. In a sense, the groove in the MK model is an idealized form of the inhomogeneous nature of plastic properties of the sheet, and from consideration of a large number of groove orientations, the weakest direction in the sheet with respect to localized necking resistance can be retrieved.

The accuracy in the right-hand side of the FLD has increased over the years by improvements of the constitutive behaviour. It was recognised, e.g. in Hutchinson and Neale (1977b), that taking strain-rate sensitivity into account shifts the Forming Limit Curve (FLC) to higher major strain levels in better accordance with experiments. This effect is even significant for materials with low strain-rate sensitivity, such as steels (Ghosh (1977)). The use of more realistic yield loci results in an improved shape of the predicted FLC in the right-hand side of the FLD. In Barlat (1989), different isotropic yield loci were used in an MK model: i.e. the polycrystalline Taylor-Bisshop-Hill yield loci for random crystallographic texture, using fcc

or bcc slip systems. They produce FLCs that are quite realistic compared to the Tresca and von Mises yield loci which result in gross under- or overestimation, respectively. The significance of the yield surface shape for the right-hand side of the FLD is further explored in Lian et al. (1989), where it is shown that the FLC shape is strongly related to the yield surface shape between plane strain deformation and equibiaxial stretching. The stress increase during the strain path change towards plane strain of the groove in the MK model results in a delay in the onset of necking in the right-hand side of the FLD. These authors proposed the 'yield surface shape hardening diagram', which is derived from the yield locus, to assess the delay of necking in this region of the FLD. In Yao and Cao (2002), mixed isotropic-kinematic material hardening is considered within an MK analysis. It is shown that forming limits are also sensitive to anisotropic hardening, modelled by the kinematic shift of the yield locus.

In recent years, physical plasticity models have been used within the MK framework, e.g. in Knockaert et al. (2002), which uses a rate-independent polycrystal plasticity model with Taylor homogenization scheme. Such material modelling allows taking the evolution of the crystallographic texture during forming into account, and is a further improvement in the accuracy of FLC predictions. Different studies on this topic indicate that it depends on the initial texture whether or not formability is influenced by texture evolution. In Inal et al. (2005), employing a rate-sensitive elasto-plastic polycrystal plasticity model, the effect of texture evolution on formability was found to be negligible, while in Tóth et al. (1996), the study of the formability of three aluminium textures shows the tendency to equalize the forming limits of the different textures and lower them when texture development is considered. This last study uses the rate insensitive Taylor approach of polycrystal plasticity. The effect of the cube texture component in aluminium is studied with a rate-dependent plasticity model in Wu et al. (2004), where it was found that the spread around the ideal texture component determines whether or not formability is influenced by texture evolution

under equibiaxial stretching. Signorelli et al. (2009) use a viscoplastic self-consistent (VPSC) polycrystal material model within the MK framework. It is demonstrated that the different textural evolutions associated with a difference in initial texture, can shift the right-hand side of the predicted FLC up- or downwards to a significant extent. It is also seen that a higher grain aspect ratio in the VPSC model reduces limit strains in the right-hand side of the FLD. In Neil and Agnew (2008), dislocation-based plasticity as well as mechanical twinning of a Mg alloy (hcp) is considered, at different elevated temperatures, within the framework of a VPSC material model. It is found that twinning can promote the resistance to localized necking.

Although the FLD is a widely spread tool in press shop practice, it has its limitations. In its original form, it can not be used for formability predictions under non-monotonic loading conditions, for sheets which are bent during forming, and for sheets subjected to non-zero stresses normal to the sheet plane during forming. Insights in these limitations have been established in the past through the MK model concept, as discussed next.

In an extensive study by Barata da Rocha (1989), it is found that under equibiaxial stretching followed by uniaxial tension, formability is dramatically lower compared to the monotonic FLD, while much higher limit strains are obtained under uniaxial tension followed by equibiaxial stretching. As reported in this paper, the same trends are also found in experimental investigations. In Hiwatashi et al. (1998), the effect of anisotropic hardening at strain path changes (due to dislocation substructure development), is assessed with the hardening model of Teodosiu-Hu combined with a model for texture-based anisotropy. Anisotropic hardening after a strain path change, including transient hardening, is found to have a significant effect on subsequent formability. In a recent study of Yoshida and Suzuki (2008), the connection between anisotropic hardening at strain path changes (model of

Teodosiu-Hu) and the path dependency of the Forming Limit Stress Diagram (FLSD) was shown by investigation of the forming limit stress under 2-step strain paths obtained with a MK model. The path independency of the FLSD only holds in the case that the sheet material shows isotropic hardening after a strain path change; when it shows anisotropic hardening however, the FLSD gives an over- or underestimate of the predicted forming limit, depending on whether there is a decline or increase of hardening after the strain path change, respectively. The same conclusions are drawn in Yoshida and Kuwabara (2007), but based on the measurement of stress in tubular sheets subjected to a combination of axial loading and internal fluid pressure.

In order to introduce the effect of sheet curvature in a MK-type analysis, Shi and Gerdeen (1991) introduced a strain gradient term in the constitutive hardening law. Their results show the same trends as found in various experimental studies on the influence of punch curvature between the Nakazima and Marciniak forming limit tests, i.e. a curved sheet has higher forming limits.

MK models usually assume a zero normal stress in the sheet thickness direction. This assumption is not valid for forming processes in which a hydrostatic pressure is applied during forming. Recently, the effect of the hydrostatic pressure on formability has been investigated by Wu et al. (2008), using the MK model framework. Higher forming limits in hydrostatic pressure-supported processes are predicted, which has also been observed experimentally.

Sheet metal formability is often, but not always, limited by the onset of localized necking. Chien et al. (2004) extended the MK framework in order to also consider shear instability, besides localized necking instability. The shear instability is triggered by the assumption of a band of higher initial damage with an oblique orientation with respect to the sheet normal, and

situated within the groove of an MK model. Geometric compatibility and force equilibrium between this band and the surrounding groove material is enforced. Their model is justified on the basis of the fractographic observation of an aluminum alloy that shows shear instability within a shallow neck.

In this paper, it is investigated how and why the onset of localized necking can be affected by (plastic) Through-Thickness Shear (TTS), also known as out-of-plane shear. Some publications have been made on TTS in the Single Point Incremental Forming (SPIF) process. Finite Element (FE) simulations (Eyckens et al. (2007)) and experimental studies (Allwood et al. (2007), Eyckens et al. (2008)) indicate the presence of TTS in SPIF processes.

In this paper, first the proposed generalized MK theory is developed, in essence through the addition of a new force equilibrium condition and new geometric compatibility conditions to those of a 'conventional' MK model (Hiwatashi et al. (1998)). Next, FLDs are presented, showing forming limits under monotonic deformation modes that include TTS. Finally, the formability under some selected deformation paths is discussed in more detail to explain the effect of TTS on formability in a qualitative way.

2　MODEL DESCRIPTION

2.1　CONVENTIONAL MK MODEL

The conventional MK model, i.e. as presented in Hiwatashi et al. (1998), is revisited next. In this forming limit model, the existence of a groove b with diminished thickness in a homogeneously deforming matrix a is assumed, as shown in Figure 1.

The initial imperfection f_0 is defined as

$$f_0 = \theta_0^b \big/ \theta_0^a \tag{1}$$

in which θ_0^x is the initial thickness; the superscript x refers to either the matrix a or groove b.

The velocity gradient of the matrix, expressed in the x_1-x_2-x_3 reference system, is denoted $[\mathbf{L}^a]$ and has the following form for an incompressible material subjected to a monotonic deformation:

$$[\mathbf{L}^a] = \begin{bmatrix} 1 & 0 & 0 \\ 0 & \rho_{22} & 0 \\ 0 & 0 & -(1+\rho_{22}) \end{bmatrix} D_{11}^a \tag{2}$$

The matrix strain mode is defined by:

$$\rho_{22} = \frac{D_{22}^a}{D_{11}^a} \tag{3}$$

called the in-plane strain rate ratio. To construct the monotonic FLC, ρ_{22} is taken to be a constant in the range $-1/2 \leq \rho_{22} \leq 1$. As an example of non-monotonic loading, two-stage strain paths are considered by Hiwatashi et al. (1998) with special attention to anisotropic hardening at strain-path changes.

Because $\mathbf{L}^a$ is symmetric, it follows that the strain rate tensor of the matrix $\mathbf{D}^a \equiv 1/2(\mathbf{L}^a + (\mathbf{L}^a)^T) = \mathbf{L}^a$, while the rigid body rotation rate of the matrix $\mathbf{W}^a \equiv 1/2(\mathbf{L}^a - (\mathbf{L}^a)^T) = \mathbf{0}$. Consequently, the x_1-x_2-x_3 reference frame, shown in Figure 1, can be considered to be attached to the matrix material.

In the analysis, the velocity gradient of the groove $\mathbf{L}^b$ is calculated, which generally evolves during deformation, even under monotonic loading of the matrix. Nevertheless, during a small time increment, it is assumed to be constant. Moreover, when $\mathbf{L}^b$ is expressed in the groove reference frame G, denoted $[\mathbf{L}^b]^G$, it is assumed to be of the form:

$$[\mathbf{L}^b]^G = \begin{bmatrix} L_{nn}^b & L_{nt}^b & 0 \\ L_{tn}^b & L_{tt}^b & 0 \\ 0 & 0 & L_{33}^b \end{bmatrix} = \begin{bmatrix} D_{nn}^b & D_{nt}^b + W_{nt}^b & 0 \\ D_{nt}^b - W_{nt}^b & D_{tt}^b & 0 \\ 0 & 0 & D_{33}^b \end{bmatrix} \tag{4}$$

in which the in-plane rigid body rotation rate of the groove material is characterized by W_{nt}^b.

For an incompressible material, the groove thickness strain rate D_{33}^b is equal to:

$$D_{33}^b = -D_{nn}^b - D_{tt}^b = -D_{11}^b - D_{22}^b \tag{5}$$

The measure adopted here to characterize the strain ε^x (in either matrix or groove) is defined as the time integral of the respective strain rate tensor:

$$\varepsilon^x = \int_0^T \mathbf{D}^x \, dt \quad or \quad \varepsilon_{ij}^x = \int_0^T D_{ij}^x \, dt \tag{6}$$

in which T is the total time. The deformation of the matrix is imposed incrementally, i.e. using time increments ΔT and corresponding strain increments $\Delta\varepsilon^a = \Delta T \, \mathbf{D}^a$ for a constant $\mathbf{D}^a$. For a strain-rate insensitive material model as adopted in this paper, the scalar D_{11}^a in equation (2) may be chosen freely. For convenience, it is chosen in such a way that $\|\mathbf{D}^a\| = 1$, from which it follows that $\|\Delta\varepsilon^a\|$ is numerically equal to ΔT.

The current thickness (of matrix or groove) θ^x is defined as:

$$\theta^x = \exp\left(\varepsilon_{33}^x\right)\theta_0^x \tag{7}$$

The four unknowns $D_{nn}^b, D_{tt}^b, D_{nt}^b$ and W_{nt}^b of equations (4)-(5) are computed for each imposed matrix strain increment from the subsequent equations.

Firstly, the force equilibrium over the interface between matrix and groove is written as:

$$\theta^b \sigma_{nn}^b = \theta^a \sigma_{nn}^a \tag{8}$$

$$\theta^b \sigma_{tn}^b = \theta^a \sigma_{tn}^a \tag{9}$$

in which σ_{nn}^x and σ_{tn}^x are components of $[\boldsymbol{\sigma}^x]^G$, i.e. the true (Cauchy) stress tensor of matrix a or groove b, expressed in the groove reference frame G.

Secondly, geometrical compatibility between matrix and groove is expressed as:

$$L_{nt}^b = L_{nt}^a \tag{10}$$

$$L_{tt}^b = L_{tt}^a \tag{11}$$

in which L_{nt}^x and L_{tt}^x are components of $[\mathbf{L}^x]^G$, i.e. the velocity gradient of matrix a or groove b, expressed in the groove frame G. The other non-zero components of $[\mathbf{L}^b]^G$, i.e. L_{nn}^b, L_{tn}^b and L_{33}^b, are 'free' with respect to the corresponding velocity gradient components of the matrix. These freedoms and the geometrical compatibility conditions are schematically illustrated in Figure 2.

The groove orientation in a deformed state, determined by the angle Φ, may vary from the initial groove orientation Φ_0 due to the matrix deformation (see also Figure 1):

$$\tan(\Phi) = \exp\!\left(\varepsilon_{11}^a - \varepsilon_{22}^a\right)\tan(\Phi_0) \tag{12}$$

This also implies that the groove reference system G may rotate during the deformation.

Once a constant in-plane strain rate ratio ρ_{22} and initial groove angle Φ_0 are chosen, the strain response of the groove for each matrix strain increment follows from the 4 equations (8)-(11) with unknowns $D_{nn}^b, D_{tt}^b, D_{nt}^b$ and W_{nt}^b. In practice, this set of 4 unknowns is firstly reduced to 2 by rewriting the linear equations (10)-(11) as:

$$W_{nt}^b = L_{nt}^a - D_{nt}^b \tag{13}$$

$$D_{tt}^b = D_{tt}^a \tag{14}$$

Secondly, the 2 remaining unknowns D_{nn}^b and D_{nt}^b are determined from the nonlinear equations (8)-(9) through minimization of the functional F:

$$F\!\left(D_{nn}^b, D_{nt}^b\right) = \left(\theta^b \sigma_{nn}^b - \theta^a \sigma_{nn}^a\right)^2 + \left(\theta^b \sigma_{tn}^b - \theta^a \sigma_{tn}^a\right)^2 \tag{15}$$

The functional F depends on D_{nn}^b and D_{nt}^b since the groove stress tensor components σ_{nn}^b and σ_{tn}^b are functions of $\mathbf{D}^b$ (via the adopted constitutive law), and $\mathbf{D}^b$ depends on D_{nn}^b and

D_{nt}^b only, after substitution of equations (5) and (14) into the symmetric part of equation (4).

Also, θ^b is a function of D_{nn}^b through equations (5)-(7) and (14). After minimization, the value of F is expected to be close to 0, i.e. $F < \delta$ with δ a small positive number related to the numeric precision of the minimization algorithm. In this paper, the Fletcher-Reeves-Polak-Ribiere minimization algorithm (Press et al. (1992)) has been used.

Necking of the groove is said to occur when the necking criterion:

$$\left| D_{33}^b \right| > 10 \left| D_{33}^a \right| \tag{16}$$

is satisfied. The factor of 10 in equation (16) is rather arbitrary and any other relatively large positive number can be used. The effect of this number on the matrix necking strain is minimal, since the absolute value of the groove thickness strain rate $| D_{33}^b |$ increases very rapidly towards infinity at incipient necking.

A second criterion is also adopted, which states that necking of the groove occurs if there is no longer a solution to the nonlinear system of equations (8)-(11), i.e. when it is found that after minimization, $F > \delta$.

The second necking criterion occurs more frequently for relative large matrix strain increments, e.g. $\|\Delta\boldsymbol{\varepsilon}^a\| = 10^{-2}$, while the first is more frequent for smaller strain increments, e.g. $\|\Delta\boldsymbol{\varepsilon}^a\| = 10^{-4}$. Nevertheless very similar necking strains are found for different sizes of the chosen matrix strain increment $\|\Delta\boldsymbol{\varepsilon}^a\|$.

For any particular strain mode ρ_{22}, all initial values Φ_0 in the range [-90°;90°] are considered, with an interval of 1°. The limit strain is found as the smallest matrix strain at necking of all these initial groove orientations.

2.2 TTS-MK MODEL

In its most general form, the imposed velocity gradient of the matrix $\mathbf{L}^a$ would have 8 independent components for an incompressible material, in contrast to equation (2) which only has 2 independent components. Since the scope of the present paper is only concerned with monotonic deformations (but nonetheless arbitrary in the sense that TTS is included), the form of the matrix deformation gradient need not be so general for an appropriate choice of the x_1-x_2-x_3 reference frame in which the matrix deformation is described. This system is now defined as the frame for which

(i) the x_3-direction stays normal to the sheet plane throughout the deformation. This requirement implies that:

$$L^a_{3i} \equiv \frac{\partial v^a_3}{\partial x_i} = 0 \quad (i = 1,2) \tag{17}$$

in which $\mathbf{v}^a$ is the velocity field of the matrix.

(ii) the x_1- and x_2- directions are the principal in-plane strain directions of the matrix, by which it is meant that they are chosen so that:

$$L^a_{12} = L^a_{21} = 0 \tag{18}$$

The matrix velocity gradient $\mathbf{L}^a$ is then of the form:

$$[\mathbf{L}^a] = \begin{bmatrix} 1 & 0 & 2\rho_{13} \\ 0 & \rho_{22} & 2\rho_{23} \\ 0 & 0 & -(1+\rho_{22}) \end{bmatrix} D^a_{11} \tag{19}$$

and the symmetric part of $\mathbf{L}^a$, the matrix strain rate $\mathbf{D}^a$, is given by:

$$[\mathbf{D}^a] = \begin{bmatrix} 1 & 0 & \rho_{13} \\ 0 & \rho_{22} & \rho_{23} \\ \rho_{13} & \rho_{23} & -(1+\rho_{22}) \end{bmatrix} D^a_{11} \tag{20}$$

in which 3 quantities appear that characterize the matrix strain mode:

$$\rho_{22} = \frac{D_{22}^a}{D_{11}^a}, \ \rho_{13} = \frac{D_{13}^a}{D_{11}^a}, \ \rho_{23} = \frac{D_{23}^a}{D_{11}^a} \tag{21}$$

The strain rate ratios ρ_{13} and ρ_{23} correspond to the presence of TTS in the plane perpendicular to the minor and major in-plane strain directions, respectively. It can be noted that now the spin tensor of the matrix $\mathbf{W}^a \neq \mathbf{0}$.

Expressed in the groove reference frame G, the groove velocity gradient $\mathbf{L}^b = \mathbf{D}^b + \mathbf{W}^b$ is now assumed to be of the form:

$$\left[\mathbf{L}^b \right]^G = \begin{bmatrix} L_{nn}^b & L_{nt}^b & L_{n3}^b \\ L_{tn}^b & L_{tt}^b & L_{t3}^b \\ L_{3n}^b & L_{3t}^b & L_{33}^b \end{bmatrix} = \begin{bmatrix} D_{nn}^b & D_{nt}^b + W_{nt}^b & D_{n3}^b + W_{n3}^b \\ D_{nt}^b - W_{nt}^b & D_{tt}^b & D_{t3}^b + W_{t3}^b \\ D_{n3}^b - W_{n3}^b & D_{t3}^b - W_{t3}^b & D_{33}^b \end{bmatrix} \tag{22}$$

Since equation (5) still holds, there are 8 independent unknowns in (22), described in components of the strain rate tensor ($D_{nn}^b, D_{tt}^b, D_{nt}^b, D_{n3}^b$ and D_{t3}^b) and in components of the rate of rigid body rotation tensor (W_{nt}^b, W_{n3}^b and W_{t3}^b). Equations (6) and (7) are still used to calculate strain components and current thicknesses.

To calculate the groove velocity gradient (22), the set of force equilibrium equations (8)-(9) is extended with:

$$\theta^b \sigma_{3n}^b = \theta^a \sigma_{3n}^a \tag{23}$$

since a non-zero shear stress σ_{3n} is possible due to TTS. It can be shown that for the conventional MK model, equation (23) is implicitly satisfied, as $\sigma_{3n}^a = \sigma_{3n}^b = 0$ [1].

Also the set of geometrical compatibility conditions (10)-(11) is extended:

$$L_{3t}^b = L_{3t}^a \tag{24}$$

---

[1] For a von Mises material with isotropic hardening, it follows directly from the flow law (cfr. equation (35) with $i = 3$ and $j = n$). However, for an anisotropic polycrystal, determined by its crystallographic texture, it is required that the sheet normal (x_3-axis) is a dyad axis with respect to crystallographic orientation. For many rolled sheet materials, this is a reasonable assumption.

$$L^b_{t3} = L^a_{t3} \tag{25}$$

$$L^b_{n3} = L^a_{n3} \tag{26}$$

The additional geometric compatibility conditions and additional freedoms of the groove material are illustrated in Figure 3.

Regarding the compatibility condition (24), it can be noted that

$$L^a_{3t} = 0 \tag{27}$$

which follows from the constriction (17) on the form of the velocity gradient of the matrix $\mathbf{L}^a$. As in the conventional MK model, the groove rotation is given by equation (12).

When a constant strain ratio ρ_{22} and initial groove angle Φ_0 are chosen, the set of 8 equations (8)-(9), (23), (10)-(11) and (24)-(26) determine for each matrix strain increment the 8 unknowns $D^b_{nn}, D^b_{tt}, D^b_{nt}, D^b_{n3}, D^b_{t3}, W^b_{nt}, W^b_{n3}$ and W^b_{t3} in equation (22) (taking into account equation (5)). In practice, this set of 8 unknowns is firstly reduced to 3 by rewriting the linear equations (10)-(11) and (24)-(27) into:

$$W^b_{nt} = L^a_{nt} - D^b_{nt} \tag{28}$$

$$D^b_{tt} = D^a_{tt} \tag{29}$$

$$D^b_{t3} = L^a_{t3}/2 \tag{30}$$

$$W^b_{t3} = L^a_{t3}/2 \tag{31}$$

$$W^b_{n3} = L^a_{n3} - D^b_{n3} \tag{32}$$

Secondly, the 3 remaining unknowns D^b_{nn}, D^b_{nt} and D^b_{n3} are determined from the nonlinear equations (8)-(9) and (23) through minimization of the following functional F:

$$F\left(D^b_{nn}, D^b_{nt}, D^b_{n3}\right) = \left(\theta^b \sigma^b_{nn} - \theta^a \sigma^a_{nn}\right)^2 + \left(\theta^b \sigma^b_{tn} - \theta^a \sigma^a_{tn}\right)^2 + \left(\theta^b \sigma^b_{3n} - \theta^a \sigma^a_{3n}\right)^2 \tag{33}$$

The functional F depends on D_{nn}^b, D_{nt}^b and D_{n3}^b since the groove stress tensor components

$\sigma_{nn}^b, \sigma_{tn}^b$ and σ_{3n}^b are functions of $\mathbf{D}^b$ (via the adopted constitutive law), and $\mathbf{D}^b$ depends on

D_{nn}^b, D_{nt}^b and D_{n3}^b only, after substitution of equations (5) and (29)-(30) into the symmetric

part of equation (22). Also, θ^b is a function of D_{nn}^b through equations (5)-(7) and (11).

The same necking criteria as in the conventional MK model are adopted, and the limit strain is

found as the smallest matrix strain at necking considering all initial groove angles Φ_0 in the

range [-90°;90°] with an interval of 1°. An algorithmic chart of the solution procedure of the

newly proposed TTS-MK model is presented in Figure 4.

2.3 CONSTITUTIVE MODEL

The material (matrix and groove) is assumed to be rigid-plastic and incompressible. For the

isotropic material model under consideration, the groove reference frame G is taken as the

material reference frame for both the matrix and groove material. The isotropic von Mises

yield locus is adopted, which takes the following form in the groove reference system G,

under the assumption that the sheet normal stress $\sigma_{33} = 0$:

$$\left(\sigma_{nn} - \sigma_{tt}\right)^2 + \sigma_{nn}^2 + \sigma_{tt}^2 + 6\left(\sigma_{nt}^2 + \sigma_{n3}^2 + \sigma_{t3}^2\right) = 2f_Y^2 \tag{34}$$

in which f_Y is the uniaxial yield stress. The von Mises associated flow law (normality rule) is:

$$\sigma_{ij}' = \lambda\, D_{ij} \tag{35}$$

in which λ is the plastic multiplier and σ_{ij}' is a deviatoric stress component, given by:

$$\sigma_{nn}' = \frac{2\sigma_{nn} - \sigma_{tt}}{3} \tag{36}$$

$$\sigma_{tt}' = \frac{2\sigma_{tt} - \sigma_{nn}}{3} \tag{37}$$

14

$$\sigma'_{33} = \frac{-\sigma_{nn} - \sigma_{tt}}{3} \tag{38}$$

$$\sigma'_{ij} = \sigma_{ij} \quad (i \neq j) \tag{39}$$

Isotropic hardening is assumed, of the form:

$$\sigma_{eq} = K\left(\varepsilon_0 + \varepsilon_{eq}\right)^n \tag{40}$$

in which σ_{eq} and ε_{eq} are the von Mises equivalent stress and plastic strain respectively, and K, ε_0 and n are hardening parameters.

A further derivation is given for the plane strain deformation, i.e. $D_{22}^a = \rho_{22} = 0$ (ρ_{13} and ρ_{23} may differ from 0), for the case that the groove lies along the plane strain direction ($\Phi = \Phi_0 = 0°$). This derivation will be used further on in paragraphs 4.1, 4.3 and 4.4. In this case, the n- and x_1-directions are coincident, as are the t- and x_2-directions. From the flow law (35), and equation (37), it follows that for the matrix:

$$2\sigma_{22}^a = \sigma_{11}^a \tag{41}$$

The same holds for the groove, considering equation (14)/(29):

$$2\sigma_{22}^b = \sigma_{11}^b \tag{42}$$

3 FORMING LIMIT DIAGRAMS

Table 1 gives the material data used for the FLCs given in Figure 5.

In Figure 5, it can be seen that the FLC obtained from the traditional MK model, presented in a thick line, coincides with the FLC from the TTS-MK model for the case $\rho_{13} = \rho_{23} = 0$. In this case, equation (19), defining the imposed matrix strain path of the TTS-MK model, reduces to the corresponding equation (2) of the conventional MK model. This observation is a validation of the proposed TTS-MK model as an extension of the conventional MK model without TTS.

By comparing the FLDs in Figure 5, it is evident that formability is affected in a very different way depending on the plane(s) onto which TTS is imposed. If TTS is acting on the plane perpendicular to the major in-plane strain direction (Figure 5(a)), formability increases for all the in-plane strain modes ρ_{22} except for equibiaxial stretching ($\rho_{22} = 1$) in which case there is a small decrease. If TTS is imposed on the plane perpendicular to the minor in-plane strain direction (Figure 5(b)), forming limits are increased for $\rho_{22} < 0$, unchanged for $\rho_{22} = 0$ and (slightly) decreased for $\rho_{22} > 0$. If TTS is acting on both these planes in an equal amount (Figure 5(c)), formability is increased for all the in-plane strain modes ρ_{22} (though not as much as in the case of Figure 5(a)), except for a decrease in formability under equibiaxial stretching ($\rho_{22} = 1$). It can also be noted in Figure 5 that the minimal values of the FLCs, denoted FLC_0, only lay on the intercept of the vertical axis if the TTS is imposed on the plane perpendicular to the minor in-plane strain direction (Figure 5(b)) . In Figure 5(a), they are on the right-hand side of the FLD, while in Figure 5(c), they are on the left-hand side. The shift in FLC_0 is the result of different amounts of increase of the limit strain for different strain modes around $\rho_{22} = 0$.

All initial values Φ_0 in the range [-90°;90°] are considered (with an interval of 1°) to construct the FLCs shown in Figure 5. The limit strain corresponds to the smallest value of the matrix strain at necking for all these initial groove orientations. The corresponding initial value of the groove angle, being the critical one with respect to the onset of localized necking, is denoted Φ_0^{cr}. It evolves during deformation following equation (12), until it reaches a certain value at necking, denoted by Φ^*. Figure 6(a) and (b) present respectively Φ_0^{cr} and Φ^* for various types of TTS and all in-plane strain rate ratio's $\rho_{22} \leq 0.9$. For strain modes with $\rho_{22} \leq 0$, Figure 6(b) also includes the angle which gives the direction of zero extension in the bifurcation

analysis of Hill (1952), denoted here as Φ^{Hill}. It is calculated as (see also Stoughton and Zhu (2004)):

$$\tan\left(\Phi^{Hill}\right) = \pm\sqrt{-\rho_{22}}$$ (43)

For $\rho_{22} = 1$, Figure 6(c) shows the major in-plane necking strain ε_{11}^{*} for these types of TTS, as a function of all initial groove angles Φ_0. From equation (12) it follows that for there is no groove rotation for this case ($\Phi_0 = \Phi$). The abcis of the minimal values of the respective curves gives $\Phi_0^{cr} = \Phi^*$, while the ordinate corresponds to the forming limit strain.

For the left-handed side of the FLD ($-0.5 \leq \rho_{22} < 0$), two symmetric branches can be seen in Figures 6(a) and (b) if TTS acts on the plane perpendicular to either one of the two principal in-plane strain direction, or if TTS is absent. In these cases the resulting major in-plane necking strains are found to be symmetric around $\Phi = 0°$, i.e. $\varepsilon_{11}^{*}(-\Phi) = \varepsilon_{11}^{*}(\Phi)$. However, if TTS is present on both planes perpendicular to the two in-plane principal strain directions, this symmetry does not hold, resulting in a single branch. It can also be seen in Figure 6(b) that the Hill angle gives a reasonable approximation of Φ^* for all considered cases of TTS. Excluding equibiaxial stretching and the case $\rho_{13} = \rho_{23} \neq 0$, it was found for all non-negative in-plane strain rate ratio's ($0 \leq \rho_{22} < 1$) that $\Phi_0^{cr} = \Phi^* = 0°$. It means that the critical groove is perpendicular to the major in-plane strain direction and that there is no groove rotation during deformation (this follows directly from equation (12)). This observation agrees with the assumption of the groove orientation used in the original paper of Marciniak and Kuczynski (1967). In case TTS acts on both planes perpendicular to the two in-plane principal strain directions in an equal amount, the critical groove direction is not perpendicular but oblique to the major in-plane strain direction.

In the case of equibiaxial stretching ($\rho_{22} = 1$), each in-plane direction is a principal in-plane strain direction. As a result of this, both curves corresponding to a single non-zero TTS-strain rate ratio in Figure 6(c) are the same, apart from a horizontal shift of $\Phi = 90°$. Under equibiaxial stretching with $\rho_{13} \neq 0$ and $\rho_{23} = 0$, the value of Φ_0^{cr} is found to be 0°, while under equibiaxial stretching with $\rho_{13} = 0$ and $\rho_{23} \neq 0$, it is $\Phi_0^{cr} = \pm 90°$. The imposed strain rate of the matrix in the critical groove reference frame is in fact the same in these two cases. Under equibiaxial stretching, the observed trend is a small decrease in formability in the presence of TTS in a single plane, and a larger decrease in formability when TTS is imposed onto 2 orthogonal planes.

4   FORMABILITY OF SELECTED DEFORMATION MODES

In the subsequent paragraphs, 5 selected deformation modes are studied in more detail, 3 of which correspond to plane strain (i.e. $\rho_{22} = 0$): without TTS, with TTS in the x_2-x_3-plane and with TTS in the x_1-x_3-plane, in paragraphs 4.1, 4.3 and 4.4 respectively. In all these cases, the groove is considered to lay perpendicular to the x_1-axis before deformation ($\Phi_0 = 0°$) since it is the critical initial groove orientation, i.e. resulting in the lowest necking strain. In all these cases the groove does not rotate, so $\Phi = \Phi_0^{cr} = \Phi^* = 0°$.

Equibiaxial stretching without TTS is considered in paragraph 4.2. For this particular deformation mode, the necking strain does not depend on Φ_0, considering the isotropic constitutive law which is adopted. Also in this case, there is no groove rotation. For sake of simplicity, also $\Phi = \Phi_0^{cr} = \Phi^* = 0°$ is taken in the study. To summarize, it can be said that for the cases in the paragraphs 4.1 through 4.4, both reference frames coincide during the whole deformation, i.e. the n- and x_1-direction are aligned, as are the t- and x_2-direction. Paragraph

4.5 treats the case of uniaxial tension, i.e. $\rho_{22} = -0.5$. In this case, both reference frames do not coincide for the critical groove orientation.

4.1 PLANE STRAIN DEFORMATION WITHOUT TTS ($\rho_{22} = \rho_{13} = \rho_{23} = 0$)

For the plane strain deformation defined by $\rho_{22} = \rho_{13} = \rho_{23} = 0$ with $\Phi = \Phi_0 = 0°$, it can be shown that the only non-zero stress components (of the matrix as well as the groove), are σ_{nn} ($= \sigma_{11}$) and σ_{tt} ($= \sigma_{22}$). The stress mode of matrix and groove can thus be represented in the σ_{nn}-σ_{tt}-section of the von Mises yield locus in normalized stress space, as shown in Figure 7. Because of equations (41)-(42), the matrix and groove stress modes ($\mathbf{u}^a$ and $\mathbf{u}^b$) coincide. Considering equation (5), it is clear that the strain rate tensor $\mathbf{D}^a$, given by equation (3), has a non-zero 33-component, so it cannot be represented as a vector in the particular section shown in Figure 7. Instead, the projection of $\mathbf{D}^a$ into this plane, denoted $\underline{\mathbf{D}}^a$, is shown. The position, direction and length of $\mathbf{D}^a$ (and also $\underline{\mathbf{D}}^a$) does not evolve during the monotonic loading. At the start of the deformation, it is required from equation (8) that the groove hardens more rapidly than the matrix. This results in a higher equivalent strain in the groove according to the hardening law (40). Consequently, the groove imperfection $f = \theta^b/\theta^a$ decreases, following equations (6)-(7), which in turn affects equation (8) as the deformation proceeds. So during deformation, the groove strain rate accelerates. At the same time, the instantaneous hardening modulus $\partial\sigma_{eq}/\partial\varepsilon_{eq}$ decreases in view of the adopted hardening law (40). This also contributes to the acceleration of the groove strain rate. The forming limit is reached when one of the two necking criteria is satisfied. As derived in Chan et al. (1984) for the hardening law given in equation (40) with $\varepsilon_0 \equiv 0$, the limit strain ε_{11}^* is given by:

$$\varepsilon_{11}^*\left(\rho_{22} = \rho_{13} = \rho_{22} = 0\right) = n \tag{44}$$

Also in the conventional FLC in Figure 5 (thick line), it can be seen that for this particular deformation mode $\varepsilon_{11}^* \approx n$.

It can be concluded that for this deformation mode, the only mechanism to delay the onset of groove necking, is a continuing acceleration of the groove strain rate, for an unchanged groove strain mode.

4.2 EQUIBIAXIAL STRETCHING WITHOUT TTS ($\rho_{22} = 1$ and $\rho_{13} = \rho_{23} = 0$)

Under equibiaxial stretching defined by $\rho_{22} = 1$ and $\rho_{13} = \rho_{23} = 0$ with $\Phi = \Phi_0 = 0°$, the stress mode of matrix and groove lay in the σ_{nn} ($= \sigma_{11}$) - σ_{tt} ($= \sigma_{22}$) section, shown in Figure 8. The matrix stress mode $\mathbf{u}^a$ corresponding to equibiaxial stretching is deduced from the flow law (35) under the condition $D_{tt}^a = D_{nn}^a$, resulting in $\sigma_{tt}^a = \sigma_{nn}^a$. In contrast to the previous case, D_{tt}^a is now non-zero and the geometrical compatibility condition (14)/(29) does not imply that the stress mode of the groove $\mathbf{u}^b$ coincides with $\mathbf{u}^a$. This is illustrated in Figure 8. From the start of deformation, the groove strain rate $\|\mathbf{D}^b\|$ is larger than $\|\mathbf{D}^a\|$, so the groove stress mode $\mathbf{u}^b$ is situated more towards the plane strain point on the yield surface (marked with a cross in Figure 8).

To comply with equation (8) as deformation proceeds, it is required that the ratio $\sigma_{nn}^b / \sigma_{nn}^a$ increases, corresponding to the increased thinning of the groove. This can be achieved by (a) excess strain hardening in the groove, giving an increase in equivalent stress of the groove compared to the matrix without stress mode change (the case of the previous paragraph), and by (b) a change of the groove stress mode towards the plane strain mode without an increase in the equivalent stress. Both occur simultaneously, in such a way that the geometrical compatibility condition (14)/(29) is exactly satisfied.

For this deformation mode the conclusion is that two (simultaneous) mechanisms delay the onset of groove necking: an increase in groove strain rate, and a change in groove strain mode towards plane strain. This explains in a qualitative way why the forming limit under this deformation mode may be significantly higher compared to the plane strain deformation, in which case the groove strain mode can not change. From this, it follows that the yield locus shape, i.e. the anisotropy which is present in al real metals, is an important parameter with respect to formability under biaxial stretching. A similar analysis of this deformation mode can be found in Lian et al. (1989).

4.3 PLANE STRAIN WITH TTS IN THE PLANE NORMAL TO THE MAJOR IN-PLANE STRAIN DIRECTION ($\rho_{22} = \rho_{13} = 0$ AND $\rho_{23} \neq 0$)

For the plane strain deformation defined by $\rho_{22} = \rho_{13} = 0$, $\rho_{23} \neq 0$ with $\Phi = \Phi_0 = 0°$, it can be shown that the only non-zero stress components (of the matrix as well as the groove), are σ_{nn} ($= \sigma_{11}$), σ_{tt} ($= \sigma_{22}$) and σ_{t3} ($= \sigma_{23}$). The stress *mode* of matrix and groove can thus be represented in the normalized σ_{nn}-σ_{tt}-σ_{t3}-section of the von Mises yield locus in stress space, as shown in Figure 9.

The equations (41)-(42), also valid in this case, imply that the possible stress modes of matrix and groove are contained within the plane $\sigma_{nn} = 2\sigma_{tt}$, shown in Figure 9. In this plane, $D_{tt}^a = D_{tt}^b = 0$, so the compatibility condition (29) is satisfied. By combining the geometric compatibility conditions (24) and (25), the following non-trivial condition for the current case can be derived:

$$D_{t3}^b = D_{t3}^a \tag{45}$$

This equation plays a similar role as equation (14)/(29) in equibiaxial stretching without TTS (for clarity however, it is not illustrated in Figure 9 as is done in Figure 8). As deformation proceeds, the matrix strain mode $\mathbf{u}^a$ remains fixed while the groove strain mode $\mathbf{u}^b$ changes

(shown with a grey arrow in Figure 9) towards the plane strain point (marked with a cross in Figure 9). Meanwhile, the groove strain rate increases in such a way that the compatibility condition (45) and the force equilibrium condition (8) are exactly satisfied.

As under equibiaxial loading without TTS, the onset of necking is delayed due to a groove strain mode change towards the plain strain point. For anisotropic materials, an accurate representation of the current section of the yield loci is thus essential for an accurate description of formability under this deformation mode, a fact which is well recognized in literature for monotonic biaxial stretching (the right-hand side of the FLD), see for example Barlat (1989).

4.4 PLANE STRAIN WITH TTS IN THE PLANE NORMAL TO THE MINOR IN-PLANE STRAIN DIRECTION ($\rho_{22} = \rho_{23} = 0$ and $\rho_{13} \neq 0$)

For the plane strain deformation defined by $\rho_{22} = \rho_{23} = 0$, $\rho_{13} \neq 0$ with $\Phi = \Phi_0 = 0°$, it can be shown that the only non-zero stress components (of the matrix as well as the groove), are σ_{nn} ($= \sigma_{11}$), σ_{tt} ($= \sigma_{22}$) and σ_{n3} ($= \sigma_{13}$). The stress mode of matrix and groove can thus be represented in the normalized σ_{nn}-σ_{tt}-σ_{n3}-section of the von Mises yield locus in stress space, as shown in Figure 10.

From equations (41)-(42), it follows that the matrix and groove stress modes are restricted to the plane $\sigma_{nn} = 2\sigma_{tt}$. By combining the force equilibrium equations (8) and (23), the following relationship is obtained:

$$\frac{\sigma_{n3}^{a}}{\sigma_{nn}^{a}} = \frac{\sigma_{n3}^{b}}{\sigma_{nn}^{b}} \tag{46}$$

Both stress ratios in equation (46) remain constant throughout the deformation since the matrix stress mode does not change. By combining equations (36) and (41) and applying the flow law (35), it can be derived that this constant is $\rho_{13}/2$. Consequently, the matrix and groove stress mode are constrained to the plane $\rho_{13}\sigma_{nn} = 2\sigma_{n3}$ shown in Figure 10.

It is thus apparent that the matrix and groove stress mode are the same and remain unchanged, i.e. at the intersection point of these two planes on the normalized yield locus. This is similar to the plane strain deformation without TTS (paragraph 4.1), from which it follows that no additional formability is possible by a groove stress mode change towards the plain strain point (marked with a cross in Figure 10). As a result, ρ_{13} has no effect on formability for ρ_{22} = 0, which can also be seen in the FLCs in Figure 5(b).

4.5 UNIAXIAL TENSION (ρ_{22} = -0.5) WITH AND WITHOUT TTS

A simple analysis similar to those given in the preceding paragraphs is difficult for uniaxial loading. The critical initial groove orientation $\Phi_0{}^{cr}$ is in general different from 0° (see also Figure 6(a)), which means that the groove reference frame G does not coincide with the x_1-x_2-x_3 reference frame. Also, there is groove rotation towards the major in-plain strain direction during deformation according to equation (12). As a result, the imposed matrix velocity gradient evolves when expressed in the groove reference frame G, even though it is constant for the monotonic straining under consideration when expressed in the x_1-x_2-x_3 reference frame. The geometric compatibility and force equilibrium, expressed in the groove reference frame G, are thus of a more complex nature and more difficult to analyze.

On the one hand, the beneficial effect of all the different types of TTS on forming limits is evident in the left-hand side of the FLDs in the Figures 5(a), (b) and (c). It can be noted that, for ρ_{22} = -0.5, the effect of TTS in the plane perpendicular to the major in-plane strain direction (Figure 5(a)) is higher than the effect of TTS in the plane perpendicular to the minor in-plane strain direction (Figure 5(b)). On the other hand, it can be assessed from Figure 6 that the average value of the critical groove orientation throughout deformation, is closer to 0° (i.e. a groove perpendicular to the major in-plane strain direction) than to 90° or -90°. From these

two observations, combined with the conclusions from paragraphs 4.3 and 4.4, it seems reasonable to assume that the onset of necking is postponed through the presence of TTS in the plane containing the sheet normal direction and the groove direction. This will be discussed next in more detail.

Analogously to the definition of the strain rate ratios in equations (3) and (21), the TTS in the plane containing the sheet normal direction and the groove direction t can be characterized by:

$$\rho_{t3} = \frac{D_{t3}^a}{D_{11}^a} \tag{47}$$

More in particular, the amount of this kind of TTS, i.e. the absolute value $|\rho_{t3}|$, is relevant. From the proper tensor transformation of the strain rate tensor of the matrix $[\mathbf{D}^a]$ given in equation (20), i.e. a rotation over Φ around x_3, it is found that:

$$|\rho_{t3}| = |-\sin(\Phi)\rho_{13} + \cos(\Phi)\rho_{23}| \tag{48}$$

In case there is groove rotation, it is clear from equation (48) that $|\rho_{t3}|$ is not constant during deformation, not even for monotonic loading. It can also be noted from equation (48) that $|\rho_{t3}|(-\Phi) = |\rho_{t3}|(\Phi)$ in case one or both of the imposed strain rate ratios ρ_{13} and ρ_{23} are equal to 0. This results in symmetric branches around $\Phi=0°$ of the corresponding curves in Figures 6(a), (b) and (c). On the other hand, for $\rho_{13} = \rho_{23} \neq 0$, it follows that $|\rho_{t3}|(-\Phi) \neq |\rho_{t3}|(\Phi)$ (for $\Phi \neq 0°$), which results in an asymmetric curve around $\Phi=0°$ in Figure 6(c) and a singly-branched curve in Figures 6(a) and (b).

As an approximation, it can be stated that the delay of the onset of necking is controlled by the amount of TTS in the *fixed* plane containing the critical groove direction at the onset of necking (denoted t^*) and the sheet normal direction, the strain rate ratio of which is given by:

$$|\rho_{t*3}| = \left| \frac{D_{t*3}^a}{D_{11}^a} \right| = \left| -\sin(\Phi^*)\rho_{13} + \cos(\Phi^*)\rho_{23} \right| \qquad (49)$$

The advantage of introducing $|\rho_{t*3}|$ lies in the fact that its value does not evolve during deformation, which allows to construct Figure 11. It gives the major in-plane limit strain under uniaxial tension deformation ($\rho_{22} = -0.5$) with various types of TTS.

It can be seen in Figure 11 that, for relatively small values of $|\rho_{t*3}|$, the three curves corresponding to three different types of applied TTS, are overlapping. This indicates that it is indeed the TTS which acts in the plane formed by the groove direction and sheet normal that controls the delay of necking. However, for higher values of $|\rho_{t*3}|$, the limit strains are high and so the total groove rotation during deformation is large. Consequently, the approximation of equation (49) to represent the TTS along the current groove direction t is less accurate and depends on the type of applied TTS. This results in diverging curves in Figure 11 for higher values of $|\rho_{t*3}|$.

5   CONCLUSIONS

In this paper, the view is adopted that the groove in the Marciniak-Kuczynski (MK) type of forming limit model represents the inhomogeneity of plastic properties which exists in every real sheet. The direction of the groove which results in the lowest necking strain, also called the critical groove direction, represents the weakest material direction with respect to localized thinning resistance.

An extension to the MK forming limit model has been proposed to account for Through-Thickness Shear (TTS) during sheet metal forming. To this end, a new force equilibrium

condition and several new compatibility conditions have been introduced. For a von Mises material with isotropic hardening, various Forming Limit Curves (FLC) have been presented that feature TTS in either one or in both planes normal to the major and the minor in-plane strain directions.

The presence of TTS can influence the limit strain, ranging from a rather slight decrease to a more significant increase, depending on the strain mode. The most pronounced increase of the FLC is seen for TTS in the plane normal to the *major* in-plane strain direction.

For monotonic deformation paths in the left-hand side of the FLD, the critical groove direction is reasonably well approximated by the in-plane direction of zero extension for any case of applied TTS. In the right-handed side of the FLD, the critical groove direction is normal to the major in-plane strain direction *only if* TTS is applied onto a single plane normal to a principal in-plane strain direction, or in the absence of TTS. In the more general case, the critical groove direction is oblique.

The observation of increased formability due to TTS has been explained through the detailed study of several selected deformation modes. In summary, the case studies show that the presence of TTS in the plane defined by the critical groove direction and sheet normal, allows the assumed groove in the model to change its strain mode, resulting in delayed necking.

The process of delayed necking due to TTS is very similar to the delay in the onset of necking that is seen under a biaxial stretching mode compared to the plane strain mode, the latter case being well documented in literature. As in biaxial stretching, it is recognized that in forming processes in which TTS is present, a correct representation of the yield locus shape is crucial to make quantitative predictions of the forming limit curve which represents the onset of localized necking.

6 ACKNOWLEDGEMENT

7 REFERENCES

Allwood, J. M., Shouler, D. R., Tekkaya, A. E., 2007. The Increased Forming Limits of Incremental Sheet Forming Processes. Key Engineering Materials 344, 621-628.

Barata da Rocha, A., 1989. Theoretical Forming Limit Diagrams of Anisotropic Sheets - Linear and Non-Linear Strain Paths -. In: Forming Limit Diagrams: Concepts, Methods, and Applications, eds. Wagoner, R. H., Chan, K. S., Keeler, S. P., The Minerals, Metals and Materials Society, Warrendale, PA, pp. 183-202.

Barlat, F., 1989. Forming Limit Diagrams - Predictions Based on Some Microstructural Aspects of Materials. In: Forming Limit Diagrams: Concepts, Methods, and Applications, eds. Wagoner, R. H., Chan, K. S., Keeler, S. P., The Minerals, Metals and Materials Society, Warrendale, PA, pp. 275-302.

Boudeau, N., Gelin, J. C., Salhi, S., 1998. Computational Prediction of the Localized Necking in Sheet Forming Based on Microstructural Material Aspects. Computational Materials Science 11(1), 45-64.

Chan, K. S., Koss, D. A., Ghosh, A. K., 1984. Localized Necking of Sheet at Negative Minor Strains. Metallurgical Transactions A 15A(2), 323-329.

Chien, W. Y., Pan, J., Tang, S. C., 2004. A Combined Necking and Shear Localization Analysis for Aluminum Sheets under Biaxial Stretching Conditions. International Journal of Plasticity 20(11), 1953-1981.

Eyckens, P., He, S., Van Bael, A., Duflou, J., Van Houtte, P., 2007. Finite Element Based Formability Predictions of Sheets Subjected to the Incremental Forming Process. In: ComPlas 2007 (Proceedings of the 9th International Conference on Computational Plasticity), Barcelona, eds. Oñate, E., Owen, D. R. J., CIMNE, pp. 529-532. ISBN: 978-84-96736-27-6.

Eyckens, P., Van Bael, A., Van Houtte, P., 2008. An Extended Marciniak-Kuczynski Forming Limit Model to Assess the Influence of through-Thickness Shear on Formability. In: NumiSheet 2008 (Proceedings of the 7th International Conference and Workshop on Numerical Simulation of 3D Sheet Metal Forming Processes), Interlaken, Switserland, September 1-5, 2008, ed. Hora, P., pp. 193-198. ISBN: 978-3-909386-80-2.

Ghosh, A. K., 1977. Plastic Flow Properties in Relation to Localized Necking in Sheets. In: Mechanics of Sheet Metal Forming: Material Behavior and Deformation Analysis (1977 GMR Symposium), eds. Koistinen, D. P., Wang, N.-M., Plennum Press, pp. 287-312. ISBN: 0-306-40068-5.

Hashiguchi, K., Protasov, A., 2004. Localized Necking Analysis by the Subloading Surface Model with Tangential-Strain Rate and Anisotropy. International Journal of Plasticity 20(10), 1909-1930.

Hill, R., 1952. On Discontinuous Plastic States, with Special Reference to Localized Necking in Thin Sheets. Journal of the Mechanics and Physics of Solids 1, 19-30.

Hiwatashi, S., Van Bael, A., Van Houtte, P., Teodosiu, C., 1998. Prediction of Forming Limit Strains under Strain-Path Changes: Application of an Anisotropic Model Based on Texture and Dislocation Structure. International Journal of Plasticity 14(7), 647-669.

Hutchinson, J. W., Neale, K. W., 1977a. Sheet Necking II. Time-Independent Behaviour. In: Mechanics of Sheet Metal Forming: Material Behavior and Deformation Analysis (1977 GMR Symposium), eds. Koistinen, D. P., Wang, N.-M., Plennum Press, pp. 127-153. ISBN: 0-306-40068-5.

Hutchinson, J. W., Neale, K. W., 1977b. Sheet Necking III. Strain-Rate Effects. In: Mechanics of Sheet Metal Forming: Material Behavior and Deformation Analysis (1977 GMR Symposium), eds. Koistinen, D. P., Wang, N.-M., Plennum Press, pp. 269-285. ISBN: 0-306-40068-5.

Inal, K., Neale, K. W., Aboutajeddine, A., 2005. Forming Limit Comparisons for Fcc and Bcc Sheets. International Journal of Plasticity 21(6), 1255-1266.

Knockaert, R., Chastel, Y., Massoni, E., 2002. Forming Limits Prediction Using Rate-Independent Polycrystalline Plasticity. International Journal of Plasticity 18(2), 231-247.

Lian, F., Barlat, F., Baudelet, B., 1989. Plastic Behaviour and Stretchability of Sheet Metals. Part II: Effect of Yield Surface Shape on Sheet Forming Limit. International Journal of Plasticity 5, 131-147.

Marciniak, Z., Kuczynski, K., 1967. Limit Strains in the Processes of Stretch-Forming Sheet Metal. International Journal of Mechanical Sciences 9, 609-620.

Neil, C. J., Agnew, S. R., 2008. Crystal Plasticity-Based Forming Limit Prediction for Non-Cubic Metals: Application to Mg Alloy Az31b. International Journal of Plasticity, doi:10.1016/j.ijplas.2008.05.003

Press, W. H., Flannery, B. P., Teukolsky, S. A., Vetterling, W. T., 1992. Numerical Recipes in FORTRAN 77, second ed. Cambridge University Press, 413-420.

Shi, M. F., Gerdeen, J. C., 1991. Effect of Strain Gradient and Curvature on Forming Limit Diagrams for Anisotropic Sheets. Journal of Materials Shaping Technology 9(4), 253-268.

Signorelli, J. W., Bertinetti, M. A., Turner, P. A., 2009. Predictions of Forming Limit Diagrams Using a Rate-Dependent Polycrystal Self-Consistent Plasticity Model. International Journal of Plasticity 25(1), 1-25.

Stoughton, T. B., Zhu, X., 2004. Review of Theoretical Models of the Strain-Based FLD and Their Relevance to the Stress-Based FLD. International Journal of Plasticity 20(8-9), 1463-1486.

Tóth, L. S., Hirsch, J., Van Houtte, P., 1996. On the Role of Texture Development in the Forming Limits of Sheet Metals. International Journal of Mechanical Sciences 38(10), 1117-1126.

Wu, P. D., Embury, J. D., Lloyd, D. J., Huang, Y., Neale, K.W., 2008. Effects of Superimposed Hydrostatic Pressure on Sheet Metal Formability. International Jounal of Plasticity, doi:10.1016/j.ijplas.2008.10.002

Wu, P. D., MacEwen, S. R., Lloyd, D. J., Neale, K. W., 2004. Effect of Cube Texture on Sheet Metal Formability. Materials Science and Engineering A 364(1-2), 182-187.

Yao, H., Cao, J., 2002. Prediction of Forming Limit Curves Using an Anisotropic Yield Function with Prestrain Induced Backstress. International Journal of Plasticity 18(8), 1013-1038.

Yoshida, K., Kuwabara, T., 2007. Effect of Strain Hardening Behavior on Forming Limit Stresses of Steel Tube Subjected to Nonproportional Loading Paths. International Journal of Plasticity 23(7), 1260-1284.

Yoshida, K., Suzuki, N., 2008. Forming Limit Stresses Predicted by Phenomenological Plasticity Theories with Anisotropic Work-Hardening Behavior. International Journal of Plasticity 24(1), 118-139.

<u>Figure captions</u>

Figure 1: Scheme of the matrix a and groove b in **(a)** the undeformed and **(b)** a deformed state (with the undeformed state in dotted line). The x_1- and x_2-axes are the major and minor in-plane strain directions of the matrix, respectively. The x_3-axis (not shown) is the sheet normal. The groove reference frame G with axes n, t and x_3 is fixed to the groove and is determined by the angle Φ (in the range [-90°;90°]) from x_1 to n (denoted Φ_0 in the undeformed state). By convention, Φ is positive as drawn here.

Figure 2: Schematic illustration of the geometric compatibility conditions and freedoms of the groove velocity gradient $\mathbf{L}^b$, for the MK model in Hiwatashi et al. (1998).

Figure 3: Schematic illustration of the additional geometric compatibility conditions and additional freedoms of the groove velocity gradient $\mathbf{L}^b$ besides those shown in Figure 2, for the TTS-MK model.

Figure 4: Algorithmic chart of the TTS-MK model.

Figure 5: Forming Limit Curves for the material of Table 1, calculated using the traditional MK model (thick line) and the TTS-MK model (thin lines). In **(a)**, $\rho_{13} = 0$, while ρ_{23} has values ranging from 0.0 to 0.4. In **(b)**, ρ_{13} has values ranging from 0.0 to 0.4, while $\rho_{23} = 0$. In **(c)**, $\rho_{13} = \rho_{23}$ has values ranging from 0.0 to 0.4. The strain rate ratios ρ_{22}, ρ_{13} and ρ_{23} are defined in equation (20)-(21).

Figure 6: (a) The critical initial groove angle Φ_0^{cr} and **(b)** the critical groove angle at necking Φ^* as a function of the in-plane strain rate ratio ρ_{22} (in the range $-0.5 \le \rho_{22} \le 0.9$). **(c)** For $\rho_{22} = 1$, the major in-plane necking strain ε_{11}^* as a function of all initial groove angles Φ_0. The different curves refer to the 4 combinations of ρ_{13} and ρ_{23} shown in the legend.

Figure 7: The normalized σ_{nn}-σ_{tt}-section of the Von Mises yield locus, indicating the stress modes $\mathbf{u}^x$ and the projections of the strain rate tensor in this section $\underline{\mathbf{D}}^x$, in which the superscript x refers to the matrix *a* (printed in black) or groove *b* (printed in grey).

Figure 8: The normalized σ_{nn}-σ_{tt}-section of the Von Mises yield locus, indicating the stress modes $\mathbf{u}^x$ and the projections of the strain rate tensor in this section $\underline{\mathbf{D}}^x$, in which the superscript x refers to the matrix *a* (printed in black) or groove *b* (printed in grey).

Figure 9: The normalized σ_{nn}-σ_{tt}-σ_{n3} section of the Von Mises yield locus, indicating the stress modes $\mathbf{u}^x$, in which the superscript *x* refers to the matrix *a* (printed in black) or groove *b* (printed in grey).

Figure 10: The normalized σ_{nn}-σ_{tt}-σ_{n3} section of the Von Mises yield locus, indicating the stress modes $\mathbf{u}^x$, in which the superscript *x* refers to the matrix *a* (printed in black) or groove *b* (printed in grey).

Figure 11: The major in-plane limit strain ε_{11}^* for a number of monotonic, uniaxial tension loadings (i.e. $\rho_{22} = -0.5$), with different amounts of through-thickness shear strain rates (determined by ρ_{13} and ρ_{23}), as a function of $|\rho_{t*3}|$, defined in equation (49).

Table captions

Table 1: Material data for calculation of the FLCs.

Figure 1
Click here to download high resolution image
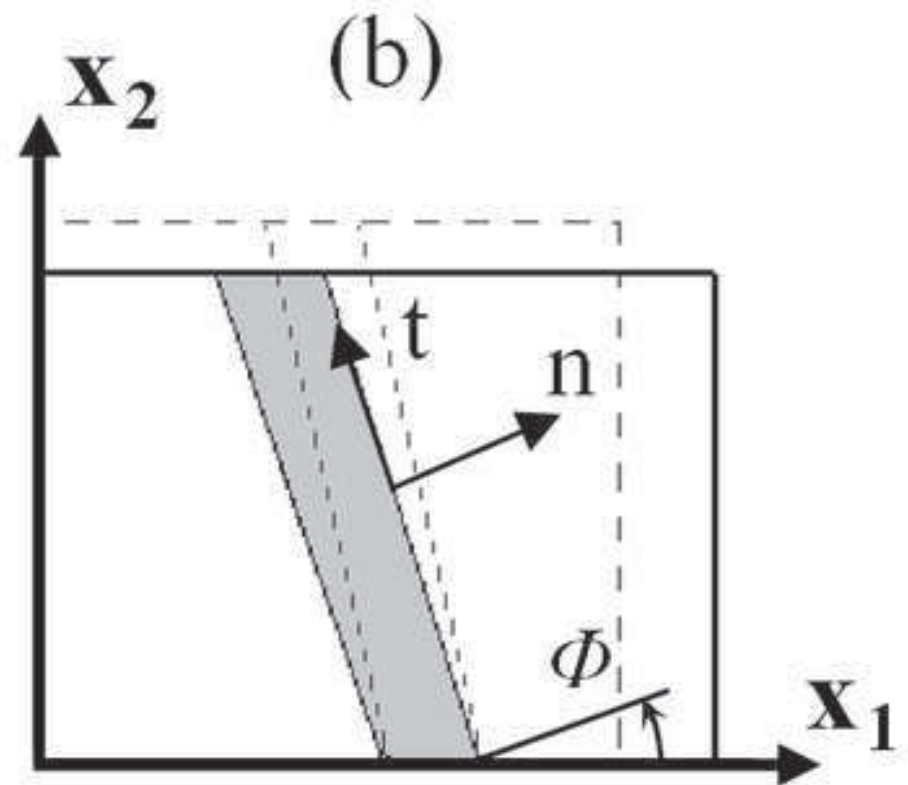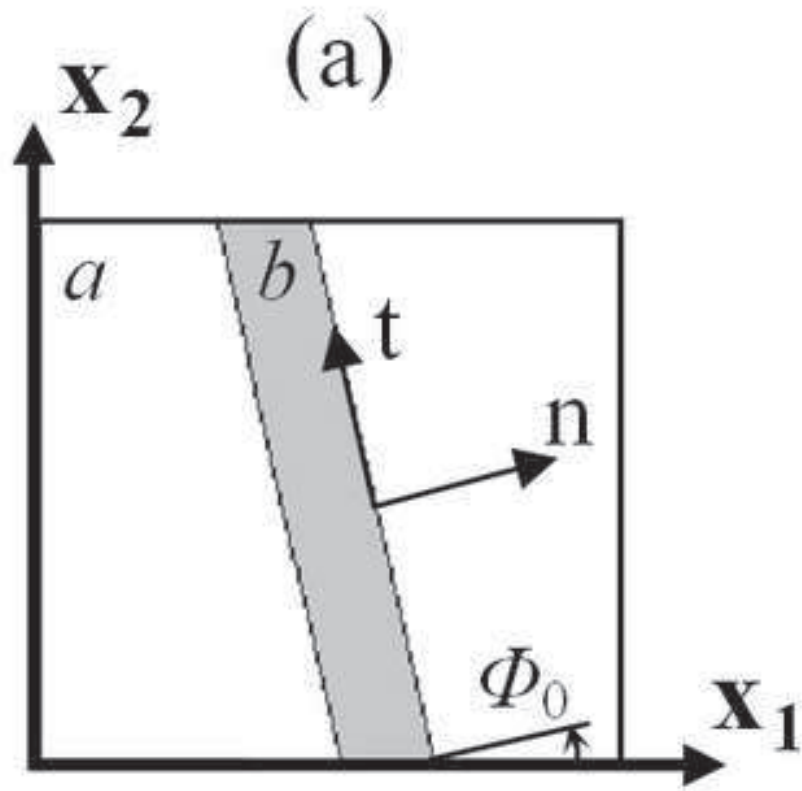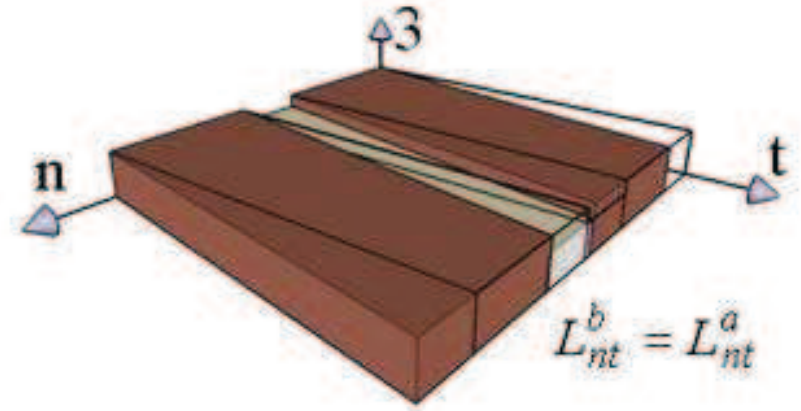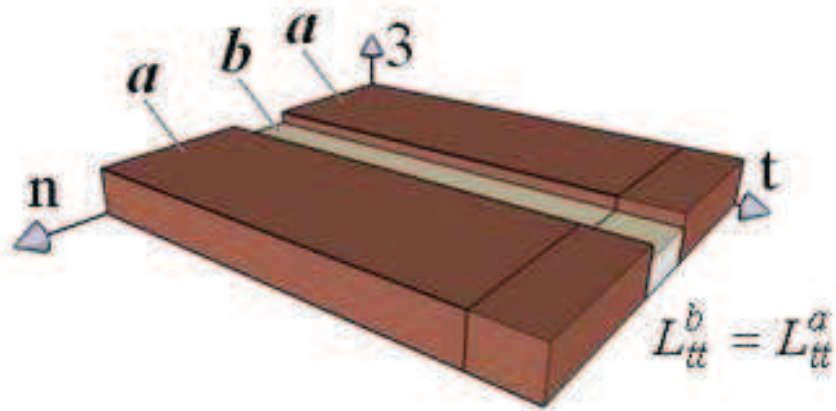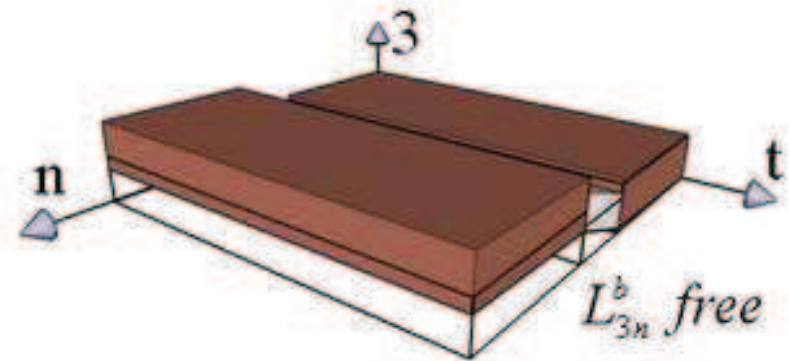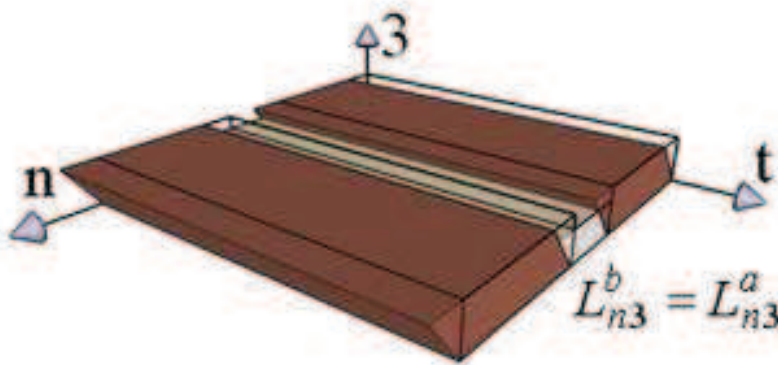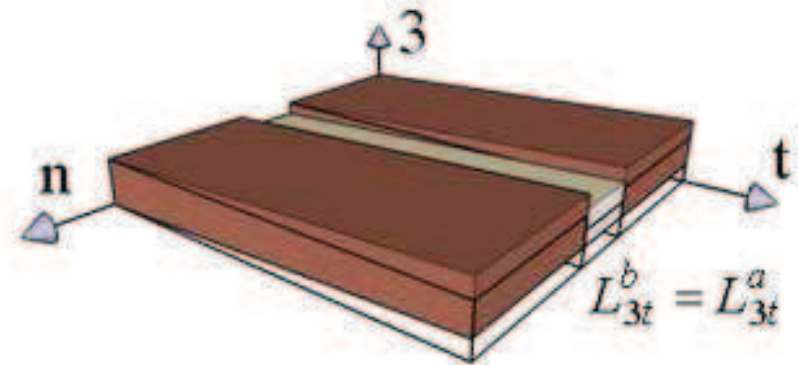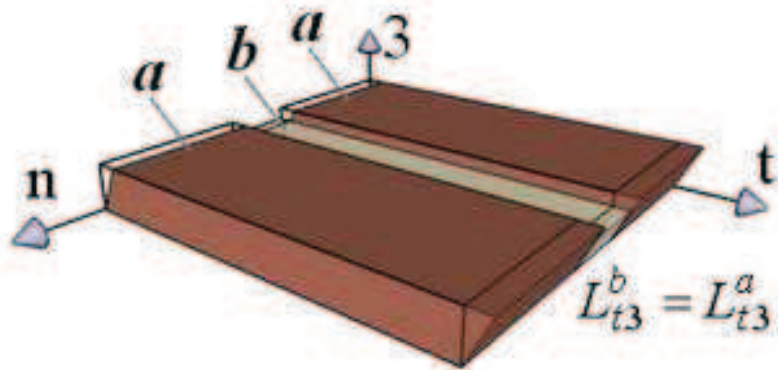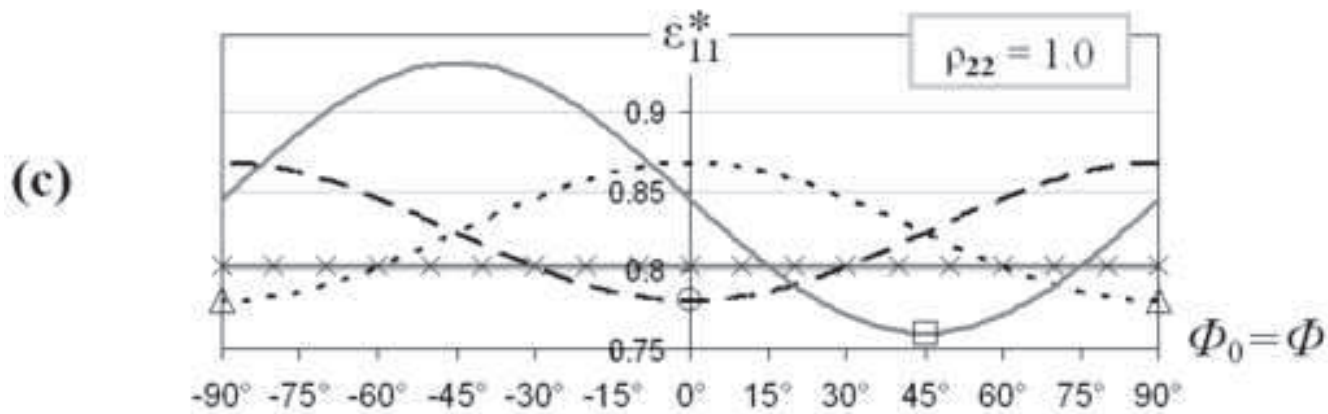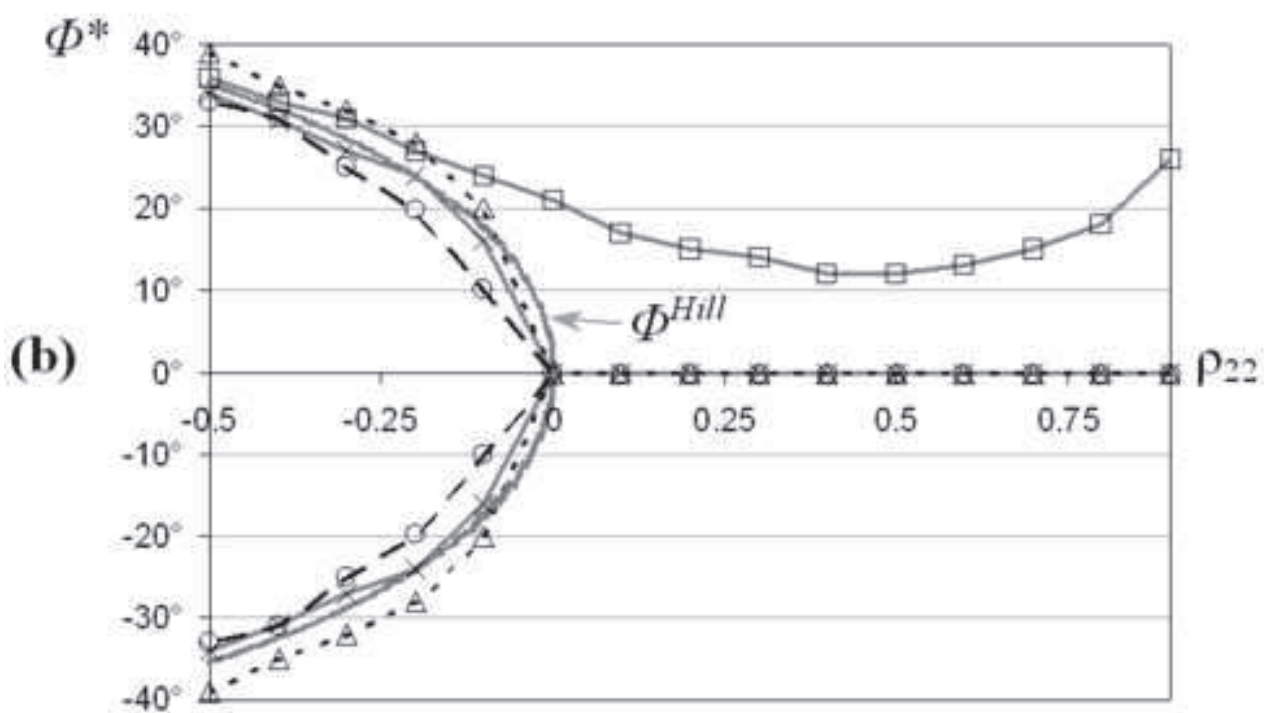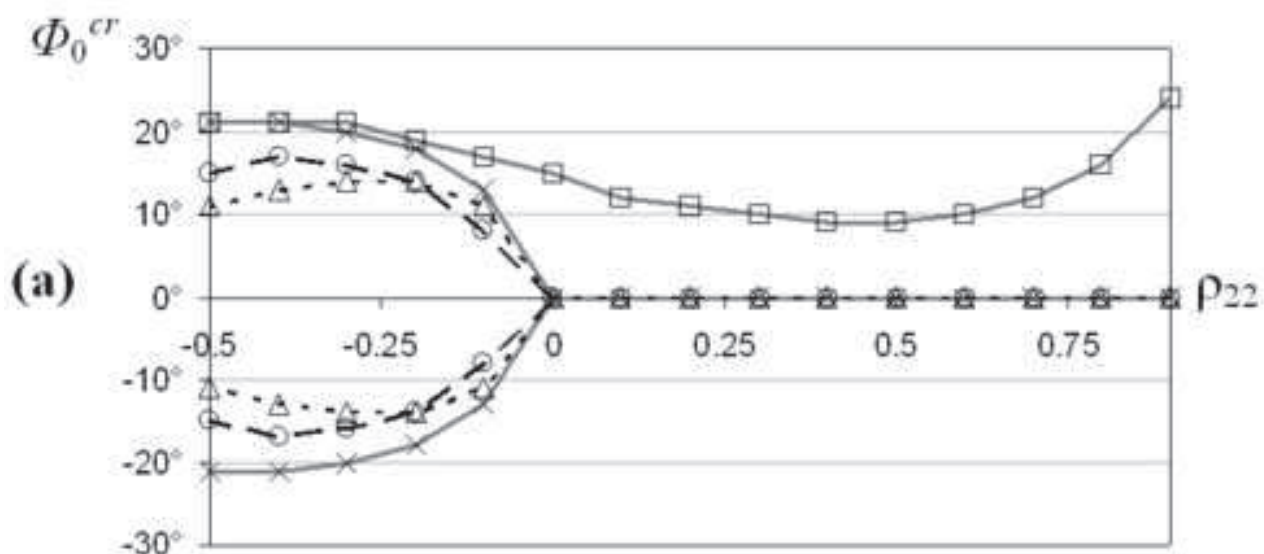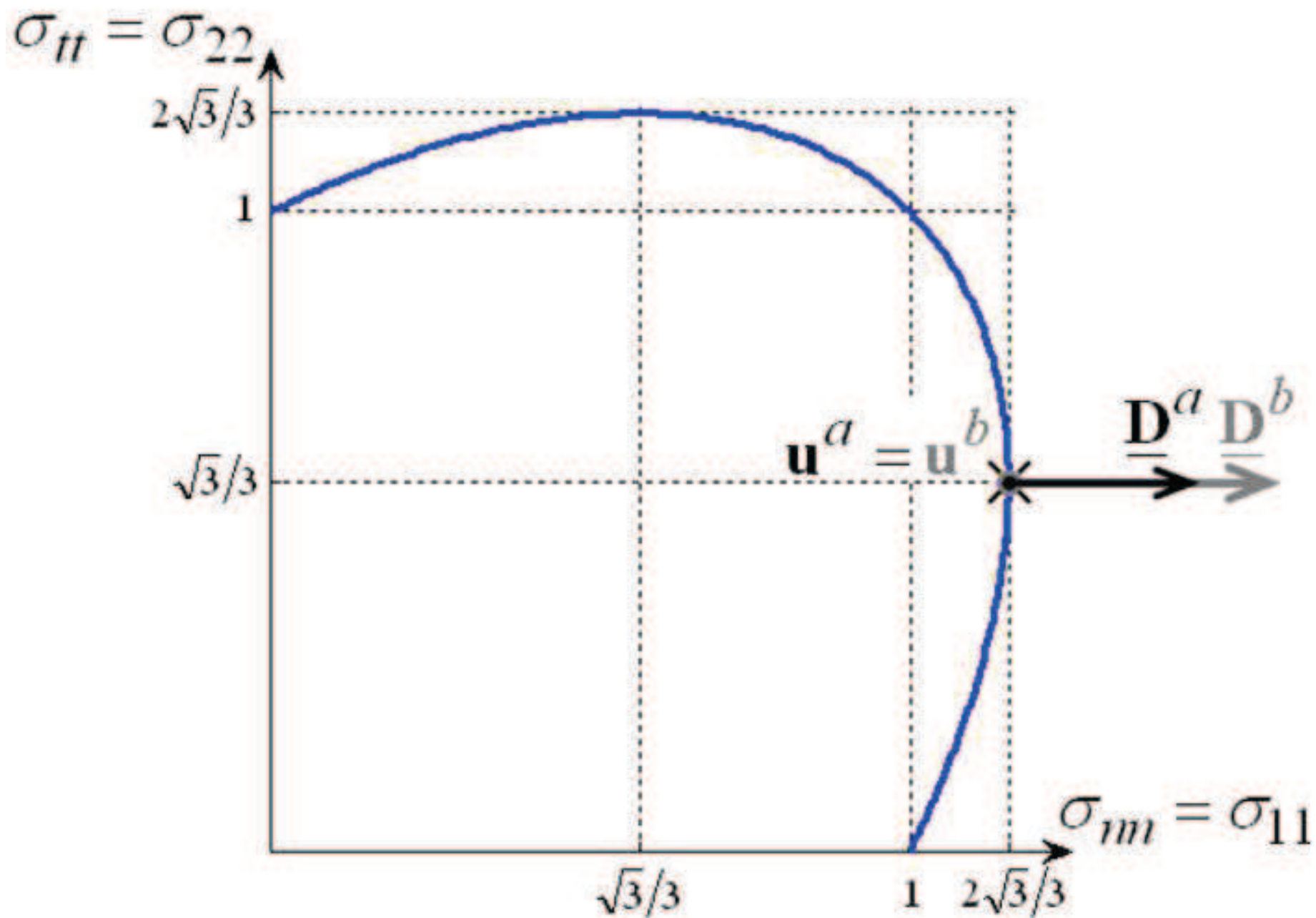
Figure 2
Click here to download high resolution image
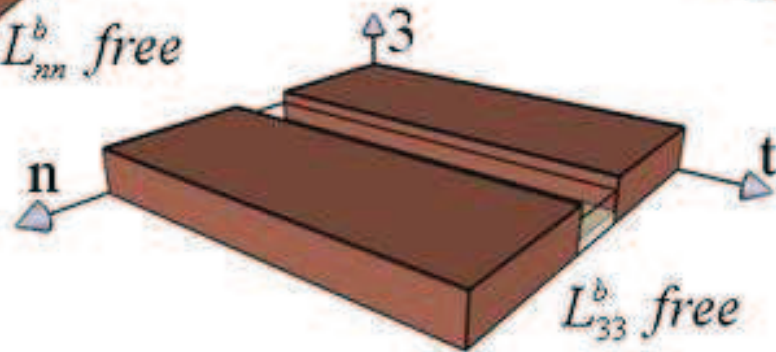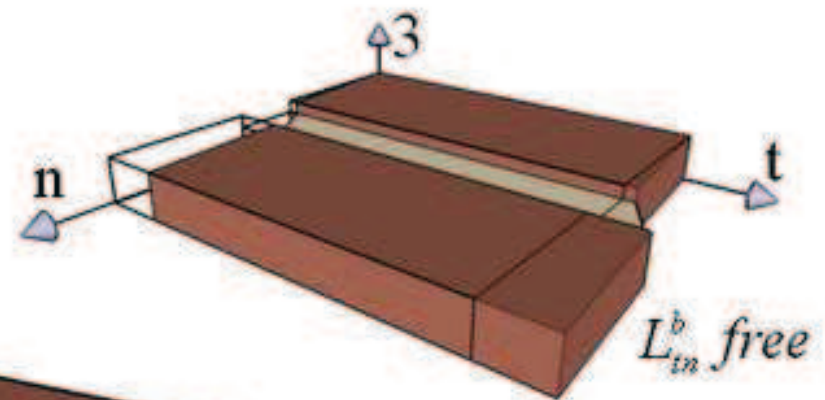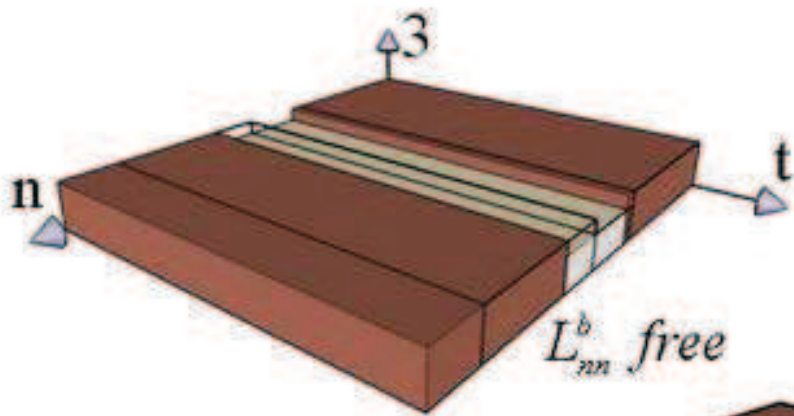
Figure 3
Click here to download high resolution image

Figure 4
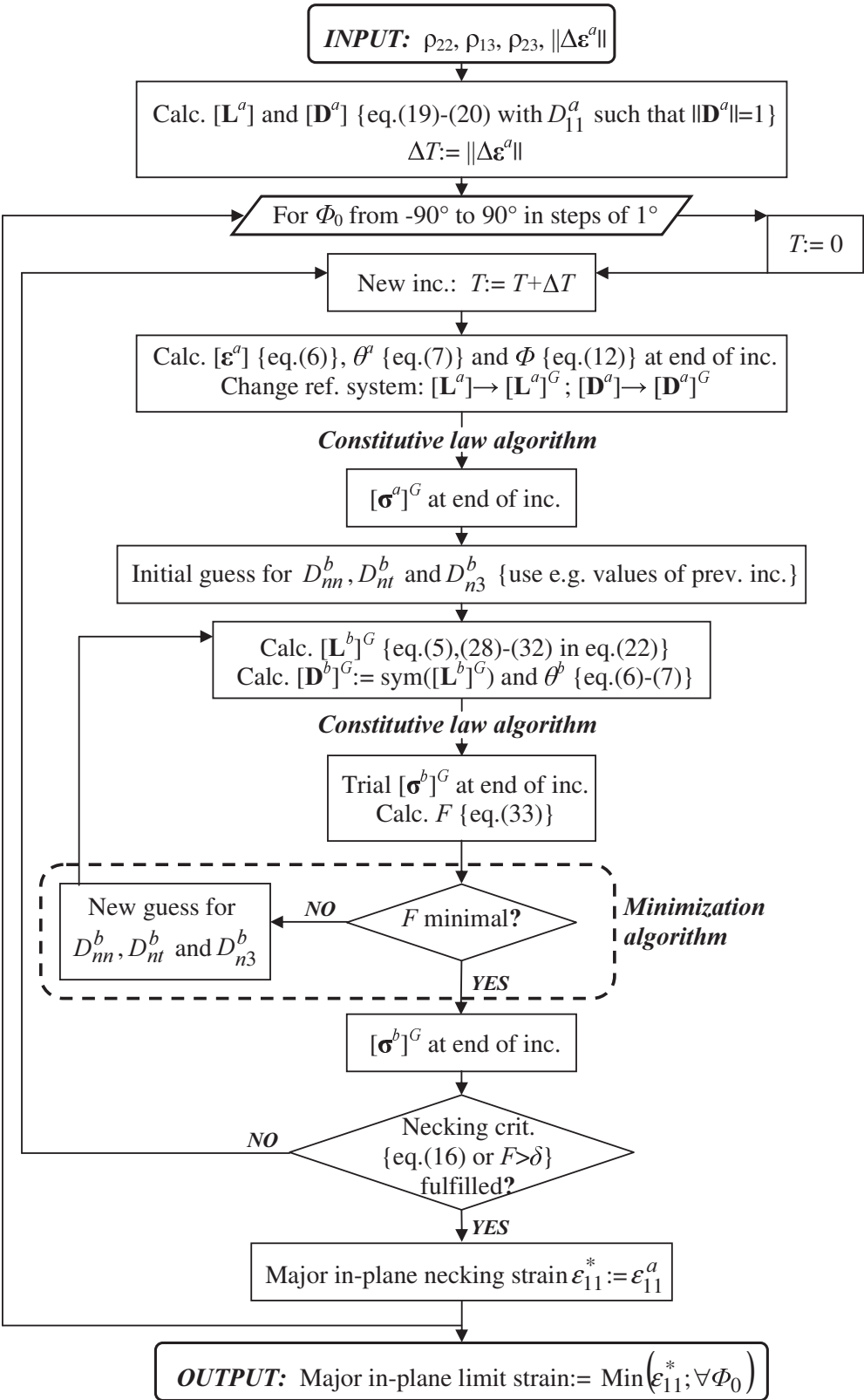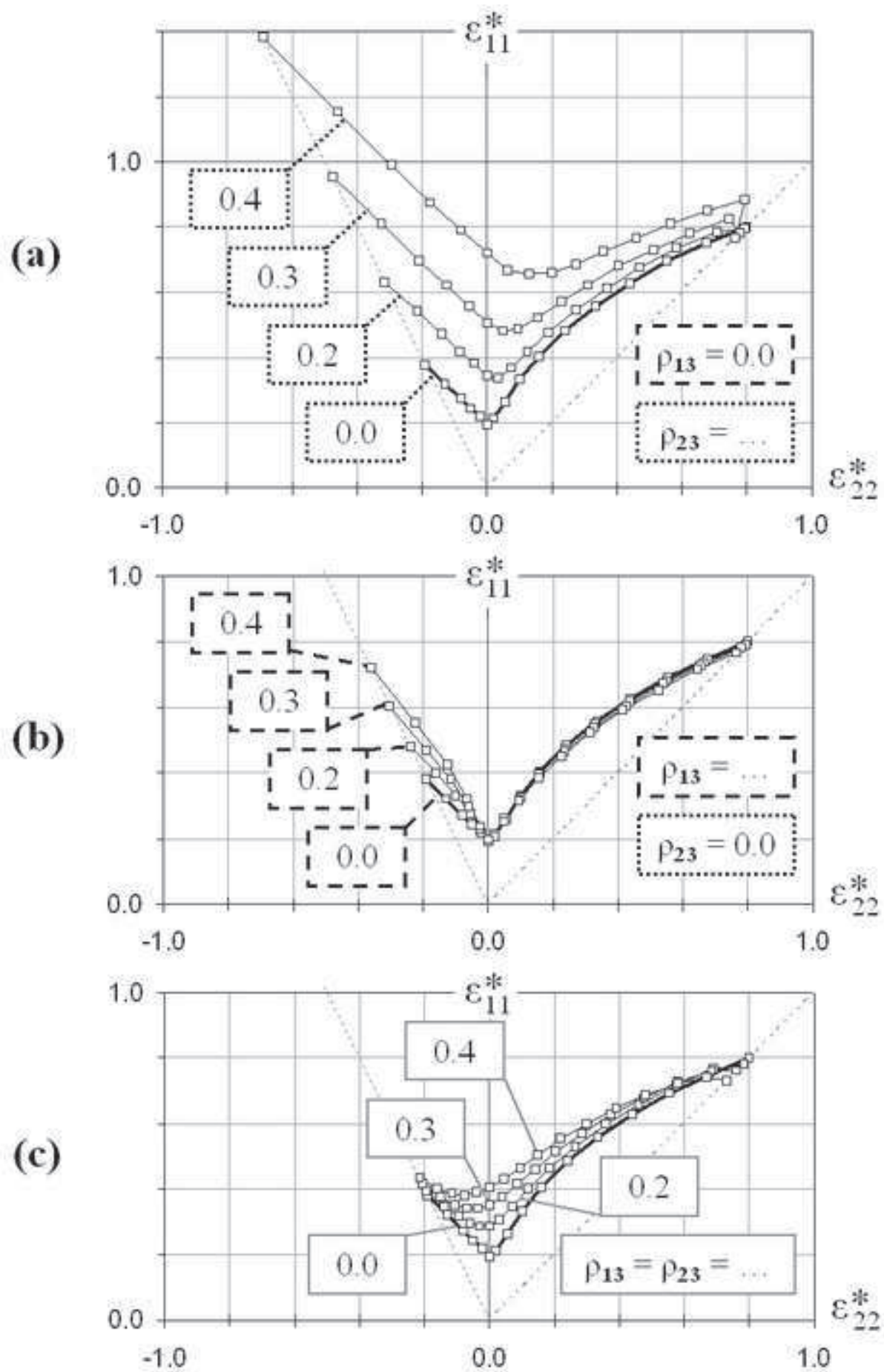
INPUT: ρ_{22}, ρ_{13}, ρ_{23}, $\|\Delta\varepsilon^a\|$

Calc. $[\mathbf{L}^a]$ and $[\mathbf{D}^a]$ {eq.(19)-(20) with D_{11}^a such that $\|\mathbf{D}^a\|=1$}
$\Delta T:= \|\Delta\varepsilon^a\|$

For Φ_0 from -90° to 90° in steps of 1°

$T:= 0$

New inc.: $T:= T+\Delta T$

Calc. $[\varepsilon^a]$ {eq.(6)}, θ^a {eq.(7)} and Φ {eq.(12)} at end of inc.
Change ref. system: $[\mathbf{L}^a]\rightarrow[\mathbf{L}^a]^G$; $[\mathbf{D}^a]\rightarrow[\mathbf{D}^a]^G$

Constitutive law algorithm

$[\boldsymbol{\sigma}^a]^G$ at end of inc.

Initial guess for D_{nn}^b, D_{nt}^b and D_{n3}^b {use e.g. values of prev. inc.}

Calc. $[\mathbf{L}^b]^G$ {eq.(5),(28)-(32) in eq.(22)}
Calc. $[\mathbf{D}^b]^G:= \text{sym}([\mathbf{L}^b]^G)$ and θ^b {eq.(6)-(7)}

Constitutive law algorithm

Trial $[\boldsymbol{\sigma}^b]^G$ at end of inc.
Calc. F {eq.(33)}

New guess for D_{nn}^b, D_{nt}^b and D_{n3}^b — NO — F minimal?

Minimization algorithm

YES

$[\boldsymbol{\sigma}^b]^G$ at end of inc.

Necking crit. {eq.(16) or $F>\delta$} fulfilled? — NO

YES

Major in-plane necking strain $\varepsilon_{11}^*:= \varepsilon_{11}^a$

OUTPUT: Major in-plane limit strain$:= \text{Min}\left(\varepsilon_{11}^*; \forall\Phi_0\right)$
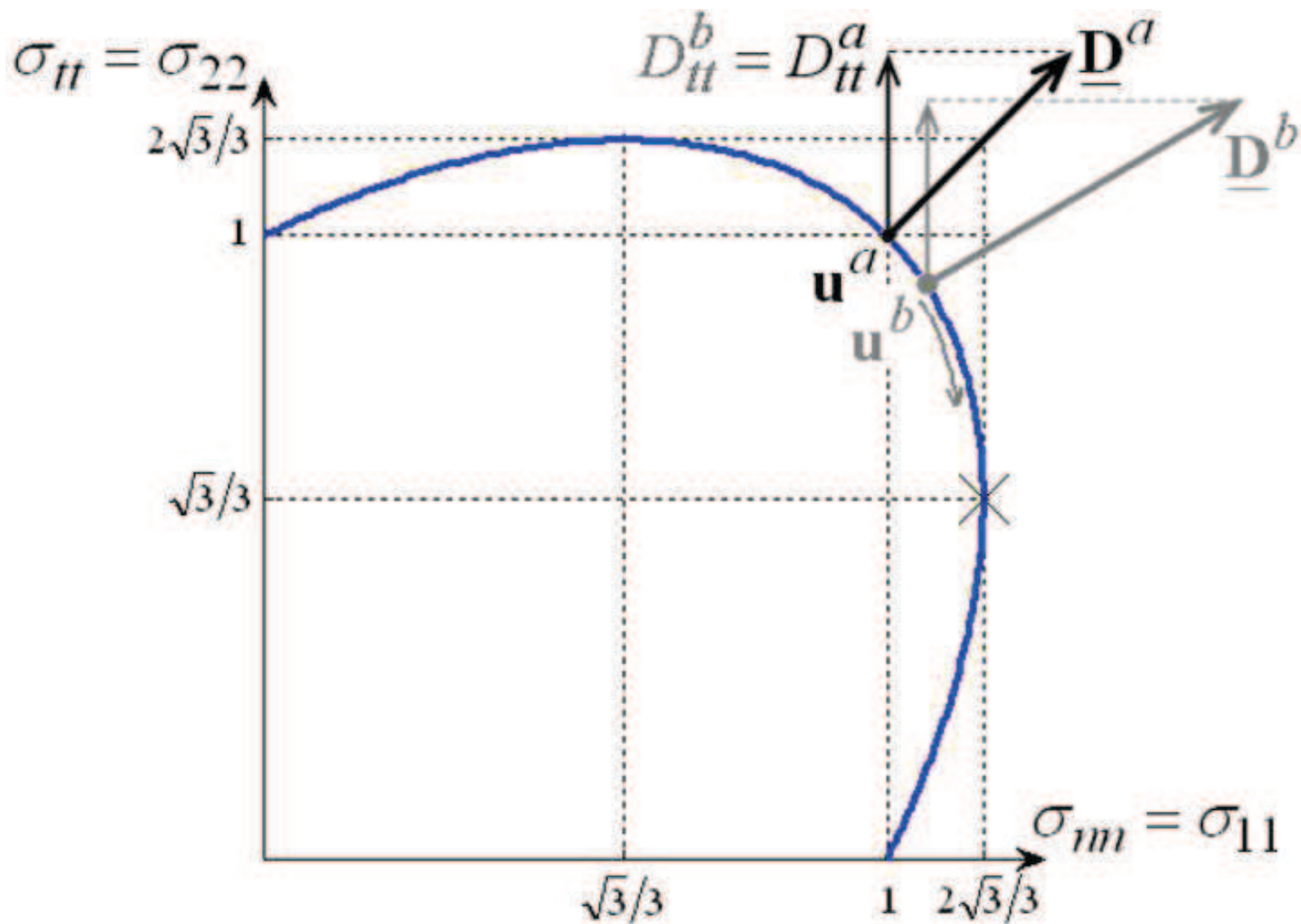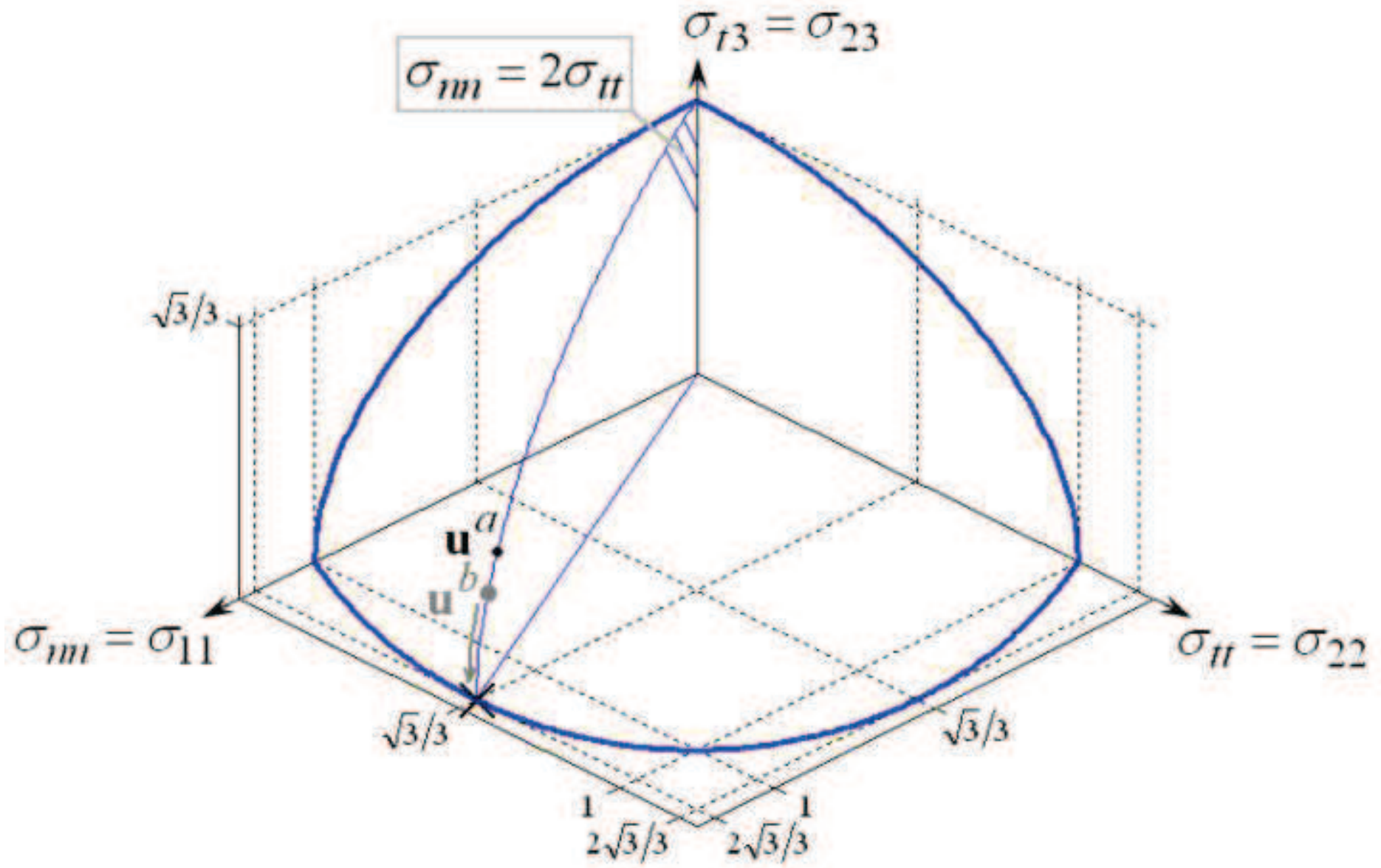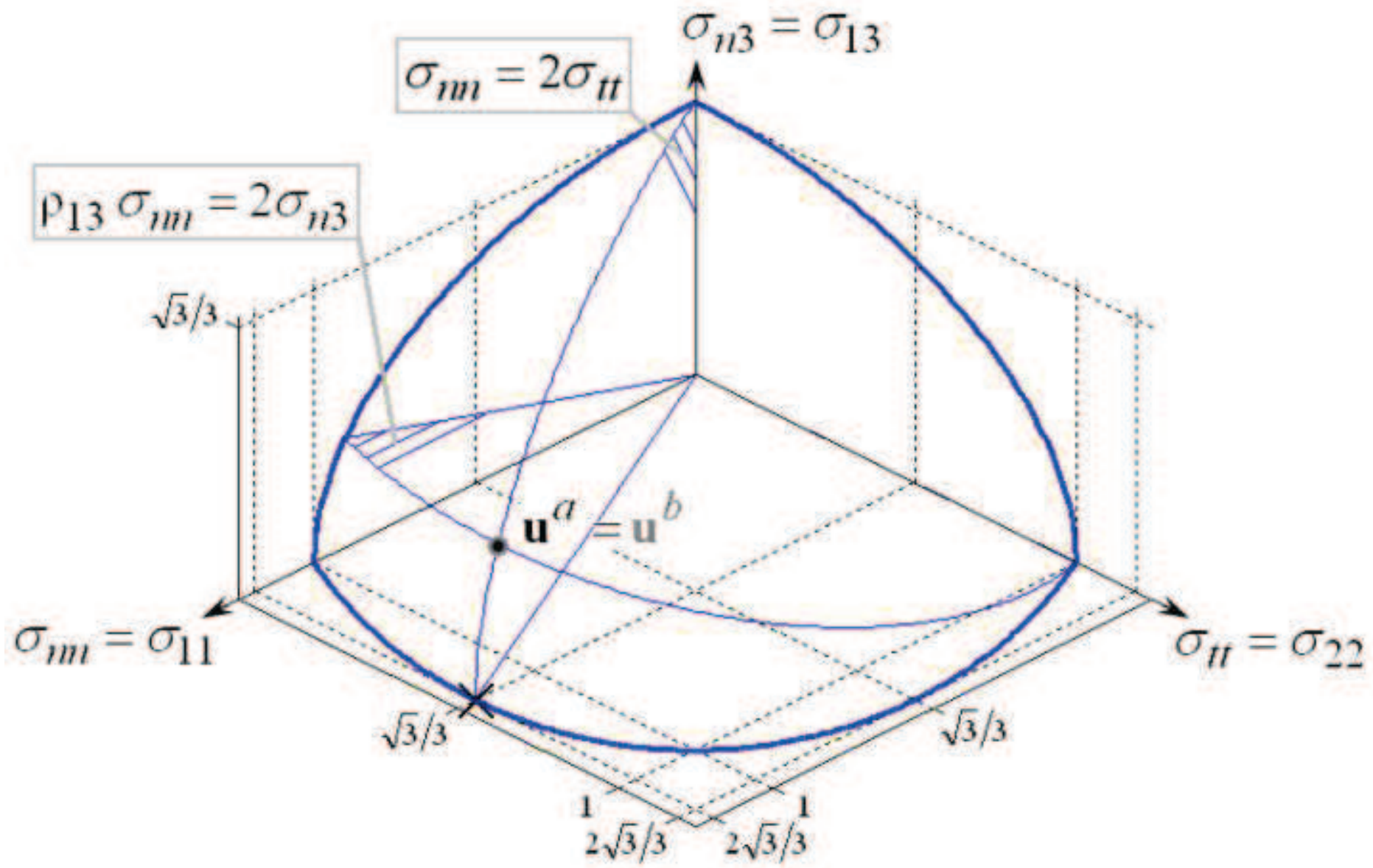
Figure 7
Click here to download high resolution image

Figure 8
Click here to download high resolution image

Figure 8

Figure 9
Click here to download high resolution image

Figure 10

Figure 11
Click here to download high resolution image
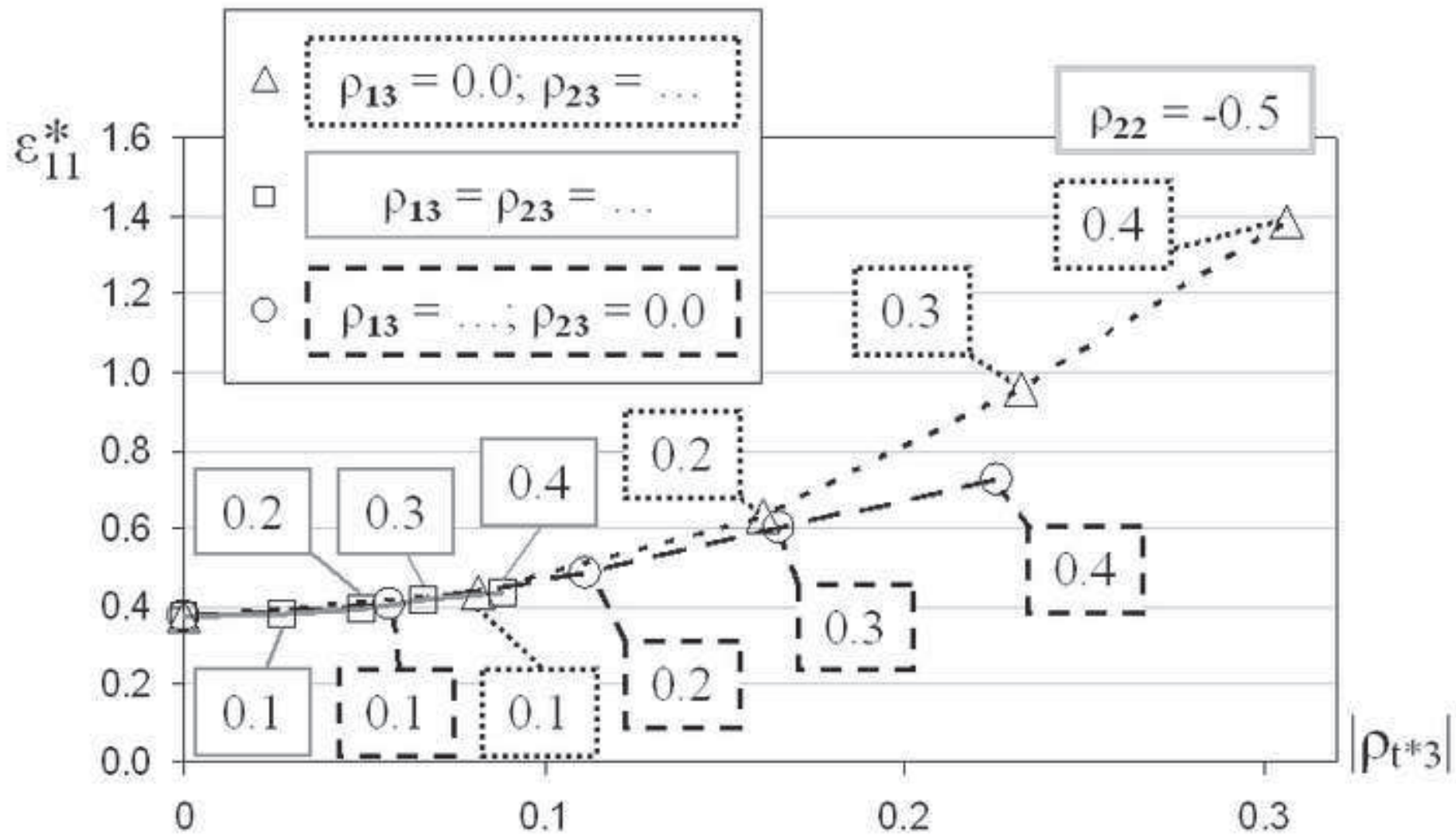
Table 1

	AA3003
f_0	0.998
K [MPa]	184.0
ε_0	0.00196
n	0.224